Chapter 5
Flash Sintering

5.1 Principle of Flash Sintering

In the past few years, flash sintering has attracted significant attention as a field-assisted phenomenon and a promising technological process [1]. The fundamental aspect of flash sintering that makes it interesting for the sintering science is a unique mechanism of the influence of electric field on densification. The important applied aspects of flash sintering include energy saving and dramatic shortening of the processing times in the technological processes of sintering. In the originally proposed format, flash sintering is based on the application of an electrical potential to the powder compact heated in a furnace [2–4]. Flash sintering has gained its name due to an extremely short densification process (a few seconds). Cologna et al. [2] reported sintering of yttria-stabilized zirconia at 850 °C within less than 5 s. This term was previously used to refer to sintering processes conducted within several minutes [5]. A DC or AC potential is applied when the sample reaches a certain temperature through furnace heating. The characteristic field strength and power dissipation values in flash sintering are 100–100 $V \cdot cm^{-1}$ and 10–1000 $W \cdot cm^{-3}$, respectively. Flash sintering has been demonstrated for oxide ceramic materials with ionic [6–9] and electronic conductivities [10, 11] as well as for non-oxide ceramics [12–17]. An Al alloy was reported to show a flash sintering behavior when a porous compact obtained by cold isostatic pressing was heated in a furnace, while copper electrodes carried a DC current to the sample [18]. In this case, the presence of oxide layers on the powder particles played a crucial role.

A schematic of the flash sintering setup is shown in Fig. 5.1. As was originally designed, flash sintering is conducted in a vertical furnace, in which a dog-bone specimen is placed in contact with platinum electrodes.

Flash sintering is accompanied by a sudden increase in the conductivity of the sintered material. It is currently agreed that the temperature (overheating) instability plays a crucial role in the development of the flash sintering. The sintering rate depends on the applied electric field; after certain field strength, the sintering process

E. A. Olevsky, D. V. Dudina, *Field-Assisted Sintering*,
https://doi.org/10.1007/978-3-319-76032-2_5

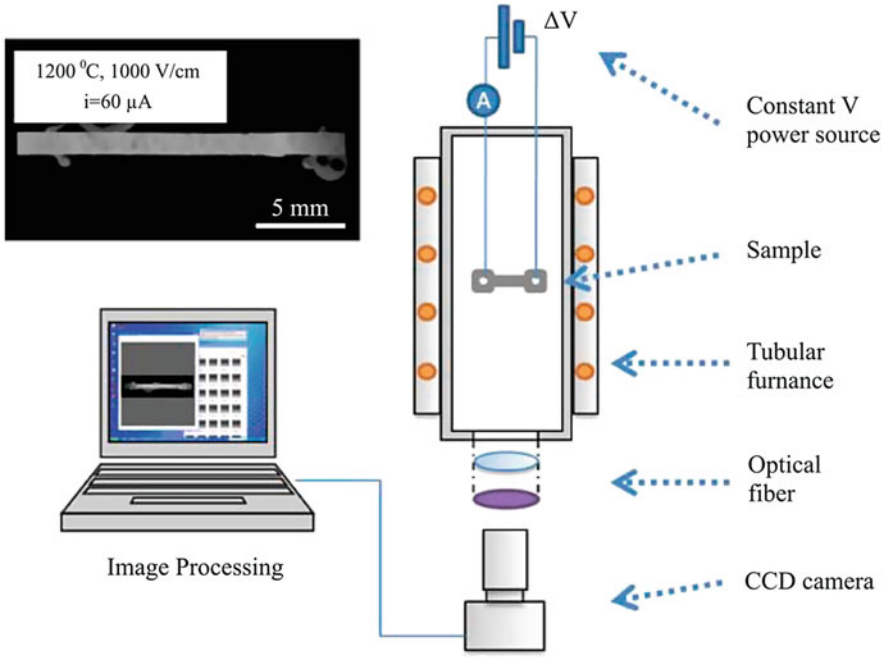

Fig. 5.1 Flash sintering setup. (Reprinted from Cologna et al. [11], Copyright (2011) with permission from Elsevier)

becomes unstable [2]. As the composition of the atmosphere can influence the conductivity of oxide materials, it can also influence the flash sintering behavior of these materials. Indeed, Zhang & Luo [19] observed a strong dependence of the onset flash sintering temperature of ZnO on the sintering atmosphere. At 300 $V \cdot cm^{-1}$, the onset flash sintering temperature of ZnO was 631 °C when sintering was conducted in oxygen, 599 °C in air, 237 °C in argon, and 186 °C in Ar + 5 mol.%H_2 (Fig.5.2a). Different onset flash sintering temperatures were explained by the dependence of the electrical conductivity of ZnO on the composition of the gaseous atmosphere. The measured conductivity of ZnO compacts versus the reciprocal of the estimated specimen temperature is shown in Fig. 5.2b for flash sintering in the four atmospheres. At 1000 $V \cdot cm^{-1}$ in a reducing atmosphere of Ar + 5 mol.%H_2, ZnO could be sintered to relative densities greater than 97% in 30 s at furnace temperatures below 120 °C. The authors emphasize that although significant lowering of the onset flash sintering temperature can be achieved for ZnO in reducing atmospheres, the temperature must still be greater than 110 °C, as at lower temperatures the interaction between hydrogen and ZnO is limited.

Hewitt et al. [20] identified incipient thermal runaway as a necessary condition for the flash event. Dong & Chen [21] showed that the onset conditions of the flash process are the same in mold-free flash sintering and mold-assisted flash sintering. Thermal runaway follows the sample's heating by means of DC or AC. The serial

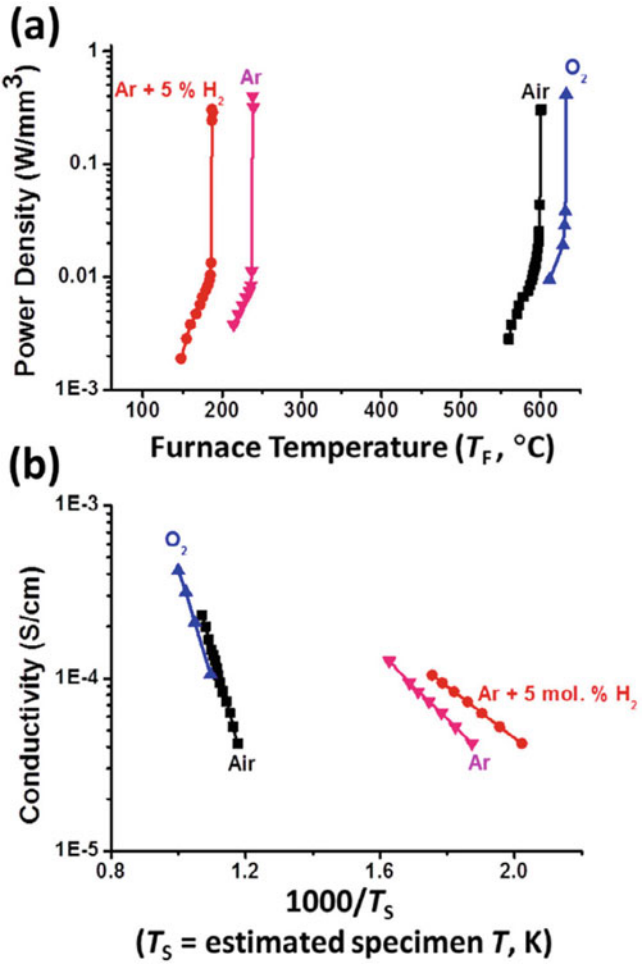

Fig. 5.2 (**a**) Measured electric power dissipation versus furnace temperature for the flash sintering of ZnO in different atmospheres at 300 V·cm^{-1}, (**b**) measured conductivity versus the reciprocal of the estimated specimen temperature. (Reprinted from Zhang and Luo [19], Copyright (2015) with permission from Elsevier)

and parallel components influence the Joule heating and conduction heat losses. In mold-assisted flash sintering, the temperature of the sample reaches a high value, but this value has a limit caused by the presence of the punches and layers of thermal insulation (Fig. 5.3). Soon after the flash, there is a drop in the voltage along the sample, as its resistance falls below those of the punches and insulations. As these conditions develop, the punches and the thermal insulation act as current limiters. So, in mold-assisted flash sintering, the maximum reachable sample temperature is limited. In both mold-free and mold-assisted flash sintering, the criterion for thermal runaway is the same: the time and temperature of thermal runaway correspond to the

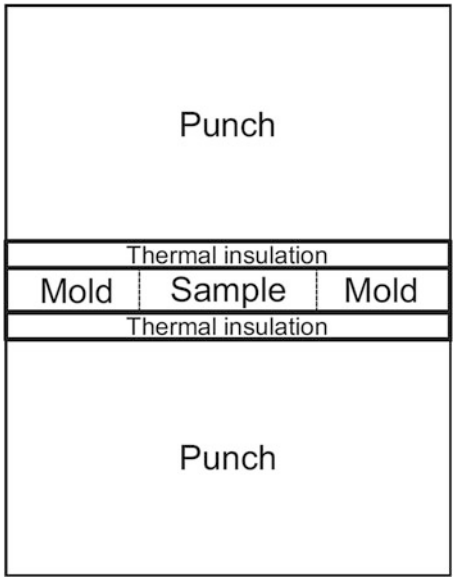

Fig. 5.3 A schematic of the assembly for mold-assisted flash sintering. (Reprinted from Dong and Chen [21], Copyright (2016) with permission of John Wiley & Sons)

moment when the Joule heating in the sample catches up with the radiation heating from the environment. When this is set as the criterion for thermal runaway, the onset temperatures of thermal runaway can be accurately predicted. For the case of mold-assisted sintering, the criterion for thermal runaway can be expressed as

$$\frac{A_s V_a^2}{H_a \rho_0 \exp\left(\frac{E_a}{k_B T_s}\right)} > \varepsilon \sigma S_{d-s} T_d^4, \tag{5.1}$$

where V_a is the voltage along the sample/mold assembly, E_a is the activation energy, ε is the emissivity, σ is the Stefan-Boltzmann constant, S_{d-s} is the surface area of the sample placed in the mold (Fig. 5.3), T_d is the mold temperature, k_B is the Boltzmann constant, T_s is the sample temperature, ρ_0 is the room temperature resistivity of the sample, H_a is the height of the sample/mold assembly, and A_s is the cross section of the sample [21].

According to Dong and Chen [21], before the onset criterion is met, the sample is heated either by radiation from the mold or from the furnace. Once Eq. (5.1) is satisfied at a certain temperature, the Joule heating will take over, and the sample will be heated further on in an accelerated manner. Thermal runaway is suppressed when at least one of the following is observed: (1) the applied voltage is below the critical voltage, (2) the sample experiences excessive thermal conduction and loses heat to the environment, (3) the conductivity of the mold is too high, or (4) the conductivity of the mold is too low. As the spark plasma sintering (SPS) machines utilize low voltages, in order to use a SPS setup as equipment for mold-assisted flash sintering, the samples should be of low height and of large diameter. An advantage of the SPS

chambers for conducting flash sintering may be the vacuum conditions and a reducing character of the sample's environment [21].

Dong & Chen suggested a simple relationship between the onset flash sintering temperature T_{on} and the applied field strength E [22]: $\frac{1}{T_{on}} \sim \log E$. A more detailed analysis allowed suggesting the following relationship [23]:

$$\ln\left(\frac{E^2}{T_{on}^4}\right) = \frac{E_a}{k_B T_{on}} + \ln\left(\frac{\varepsilon\sigma S d^2 R_0}{\beta}\right), \tag{5.2}$$

where E_a is the activation energy, k_B is the Boltzmann constant, ε is the emissivity, σ is the Stefan-Boltzmann constant, d is the sample's length, S is the sample's surface area, β is a numerical constant, and R_0 is the resistance pre-exponential factor ($R = R_0 \exp\left(\frac{E_a}{k_B T}\right)$).

Downs & Sglavo [24] have shown that cubic yttria-stabilized zirconia can be sintered in a DC electric field of 2250 V·cm^{-1} at 390 °C, which is more than 1000 °C below the sintering temperatures normally used for sintering of this ceramics. The following relationship between T_{on} and E was determined as the best fit of the experimental data:

$$T_{on}(K) = 2440 E^{-1/5.85} \left(\mathrm{V} \cdot \mathrm{cm}^{-1}\right) \tag{5.3}$$

Using this equation, the critical electric field, at which the sample enters the flash sintering regime, was calculated to be 24.5 V·cm^{-1}. This value corresponds to T_{on} equal to 1408 K. At this temperature, sintering of the chosen cubic yttria-stabilized zirconia powder starts in the absence of electric field, as was determined by dilatometry measurements. A graphical determination of the critical field is demonstrated in Fig. 5.4. The critical electric field determines the boundary between the FAST (type A) and flash (type B) sintering regimes. In type A (at low E), sintering starts at the same temperature as without the field, and the presence of the electric field only facilitates sintering by accelerating it at temperatures above 1408 K. At E, exceeding the critical value, flash sintering occurs (type B).

Analyzing the shrinkage of the samples sintered at different applied voltages, Downs & Sglavo [24] found that the compacts sintered at higher electric fields show lower linear shrinkage. Two reasons were suggested to explain the observed trend: 1) the formation of short circuit paths at high voltages and 2) the value of the current density not reaching the threshold. Based on these experiments, the authors concluded that the values of the maximum power dissipation are important for the initiation of flash sintering, but they do not determine the sample shrinkage. It is possible that a certain value of the current density needs to be reached for the uniform and efficient densification.

In their proof-of-concept paper, Saunders et al. [13] proposed a contactless version of flash sintering, in which the electric current was supplied to the sample by the arc plasma. A pre-compacted sample was placed in the gap between two pairs of plasma torches (Fig. 5.5). The sample was preheated by the plasma, and the flash

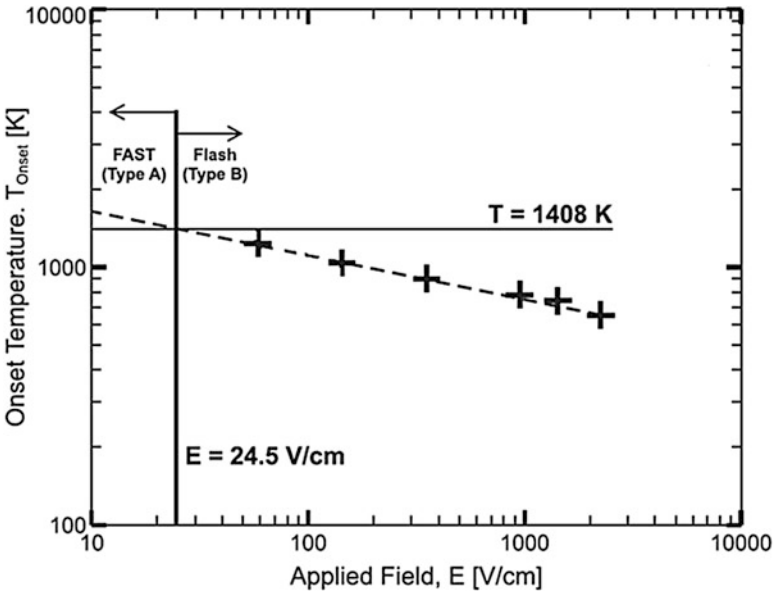

Fig. 5.4 The onset temperature of flash sintering of cubic yttria-stabilized zirconia as a log-log diagram. The dotted line corresponds to $T_{on}(K) = 2440E^{-1/5.85}$. The diagram shows a graphical method of determining the critical electric field and the boundary between the field-assisted sintering technique (FAST) and flash regimes. (Reprinted from Downs and Sglavo [24], Copyright (2013) with permission of John Wiley & Sons)

sintering itself occurred upon imposition of a flash power (Fig. 5.6). Figure 5.7 shows a general view of a B_4C–SiC sample sintered by contactless flash sintering. The compact has a dense central region after 2 s of flash sintering. In this technique, a need of direct contact of the surface of the sample with a current-carrying electrode is eliminated, and the sample can be freely moved in the gap between the electrodes. The authors emphasize that, as no electrodes are to be attached to the surface of the sample, this operation is eliminated from the sintering cycle, which becomes a great advantage of this technique over "classic" flash sintering with platinum electrodes. A transformer welder apparatus having an AC power supply was used for creating the plasma. The AC current rather than DC current was chosen to avoid a polarity-related nonuniformity of heating. Using this technique, consolidation of silicon carbide (SiC), boron carbide (B_4C), and a B_4C-SiC composite was attempted. The samples that were subjected to flash sintering were plates cut from porous compacts consolidated by (SPS). In the designed setup, conditions of flash sintering that ensure full densification of the B_4C-SiC composite and nearly full densification of single-phase B_4C were found. The geometry of the setup imposed a limitation on the sample thickness: thick samples could not be heated through the entire thickness.

A schematic of the B_4C–SiC sample subjected to contactless flash sintering in the gap between two pairs of electrodes is shown in Fig. 5.8. It was found that the

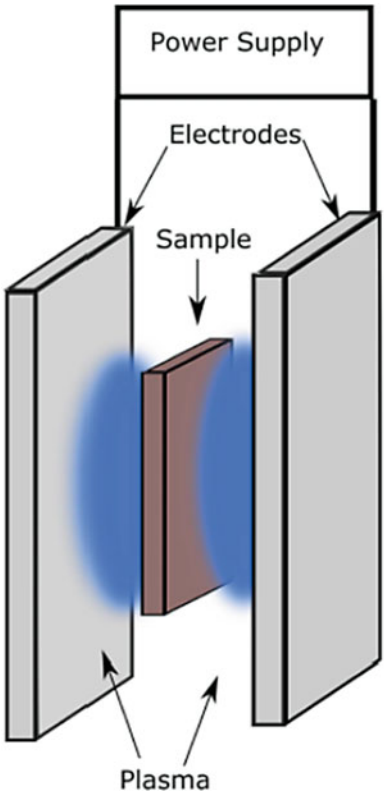

Fig. 5.5 The principle of contactless flash sintering. (Reprinted from Saunders et al. [13], Copyright (2016), Rights managed by Nature Publishing Group. This work is licensed under a Creative Commons Attribution License, http://creativecommons.org/licenses/by/4.0/)

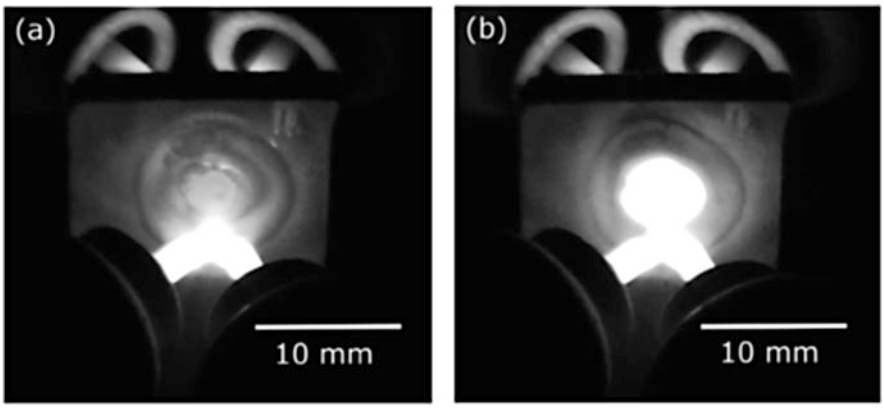

Fig. 5.6 A sample to be sintered placed in the gap between the electrodes before flash sintering (**a**) and 0.5 s after the application of the flash power (**b**). (Reprinted from Saunders et al. [13], Copyright (2016), Rights managed by Nature Publishing Group. This work is licensed under a Creative Commons Attribution License, http://creativecommons.org/licenses/by/4.0/)

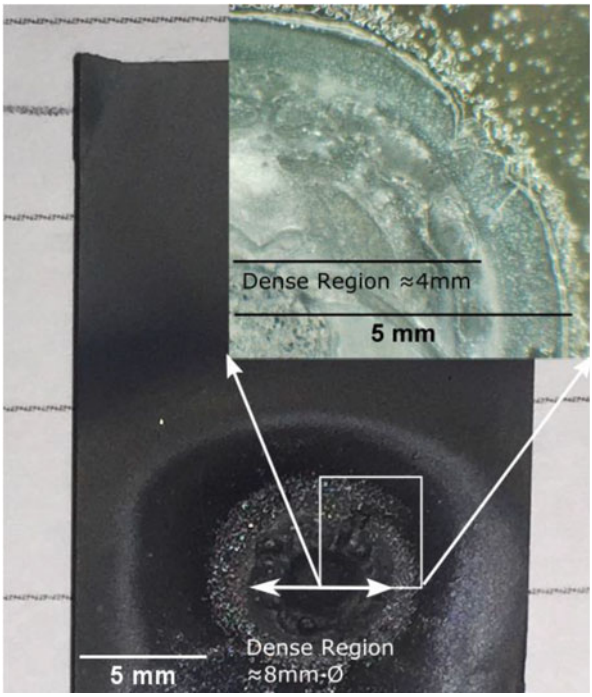

Fig. 5.7 A general view of a B_4C–SiC sample sintered by contactless flash sintering showing a dense central region; the flash sintering time was 2 s. (Reprinted from Saunders et al. [13], Copyright (2016), Rights managed by Nature Publishing Group. This work is licensed under a Creative Commons Attribution License, http://creativecommons.org/licenses/by/4.0/)

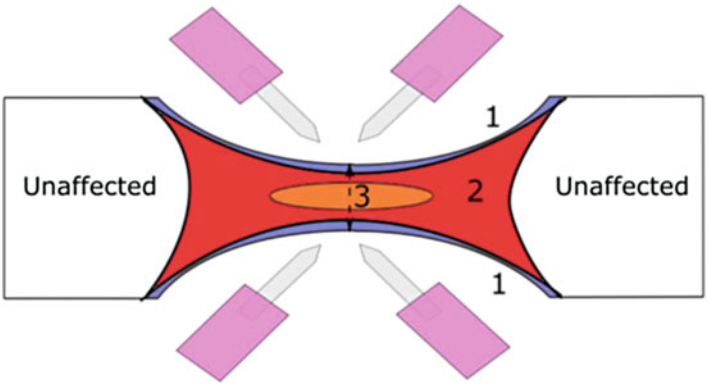

Fig. 5.8 A schematic of the B_4C–SiC sample subjected to contactless flash sintering in the gap between two pairs of electrodes (zone 1 is the zone with the highest temperature, zone 2 was densified earlier in the flash process than zone 3; as the flash sintering progressed, the boundary between zones 2 and 3 disappeared). (Reprinted from Saunders et al. [13], Copyright (2016), Rights managed by Nature Publishing Group. This work is licensed under a Creative Commons Attribution License, http://creativecommons.org/licenses/by/4.0/)

surface temperature of the sample was higher than the temperature of the interior of the sample. Zone 1 had the highest temperature and was always remelted. After 2 s from the flash sintering start, zones 2 and 3 could be distinguished by a difference between the relative densities: zone 3 has a higher porosity than zone 2. After 3 s, no difference between zones 2 and 3 could be observed, as the material was fully sintered. As the time of the flash increased, bubbles formed in zones 2–3 due to sublimation of SiC causing expansion of the material.

Flash sintering conducted using a conventional scheme is suitable for small specimens and requires platinum electrodes. Grasso et al. [14] discuss the advantages of realizing flash sintering in the SPS facilities to increase the size of the specimen, increase the productivity, and eliminate the need to use metallic electrodes. In their work, a SPS facility was successfully used for flash sintering of zirconium diboride (ZrB_2). As ZrB_2 has a higher room temperature conductivity than materials, for which flash sintering was initially developed (e.g., zirconium dioxide (ZrO_2)), it can be processed in the flash sintering mode using a low voltage. For this reason, voltages usually used in the SPS facilities are sufficient for carrying out the process of flash sintering. A pre-sintering operation was used to make a porous compact, which was placed between the punches of the assembly while no die was used. Figure 5.9 shows the displacement rate, the heating power, and the temperature developed during flash sintering of ZrB_2 with a total discharge time of 35 s.

An interesting observation was made regarding the composition of the sintered material. The initial powder of ZrB_2 contained 0.2 wt.% of carbon and 0.8 wt.% of oxygen, as the boride phase was synthesized by carbothermal reduction of ZrO_2 and the reaction was seemingly not complete. In the compact flash sintered within 35 s, substantial quantities of carbon were detected by Raman spectroscopy (Fig. 5.10a), while only negligible amounts were found in the compact produced by conventional SPS (Fig. 5.10b). In the latter, the reaction between the remaining ZrO_2 and carbon was brought to completion during sintering, and the carbon was removed in the form of carbon monoxide (CO). This example shows that full densification by flash sintering may not coincide with the synthesis completion.

Zapata-Solvas et al. [12] investigated the possibility of flash sintering of a covalent ceramic – silicon carbide (SiC). A schematic of their setup is shown in Fig. 5.11. It was possible to achieve substantial densification in a flash sintering process of SiC only when $Al_2O_3 + Y_2O_3$ additives were used. Specimen temperatures were concluded to be much higher than those in the rest of the furnace owing to direct Joule heating of the specimen; as a result, the densification near the specimen surfaces was limited by the heat losses. In pure SiC or SiC with an $Al + B_4C + C$ sintering aid, high densities of the compact were unachievable under the flash sintering conditions. Zapata-Solvas et al. [12] pointed out that the evolution of the voltage and current is affected by the temperature dependence of the resistivity of the material. The flash phenomenon was observed in all compositions — pure SiC, SiC $+(Al_2O_3 + Y_2O_3)$, and SiC$+(Al + B_4C + C)$ (Fig. 5.12). However, for each composition, there was its own range of parameters, at which flash sintering occurred. The maximum mean density of 88% was obtained for the SiC$+(Al_2O_3 + Y_2O_3)$ at an applied field of 100 $V \cdot cm^{-1}$. In pure SiC and SiC$+(Al + B_4C + C)$, densification was

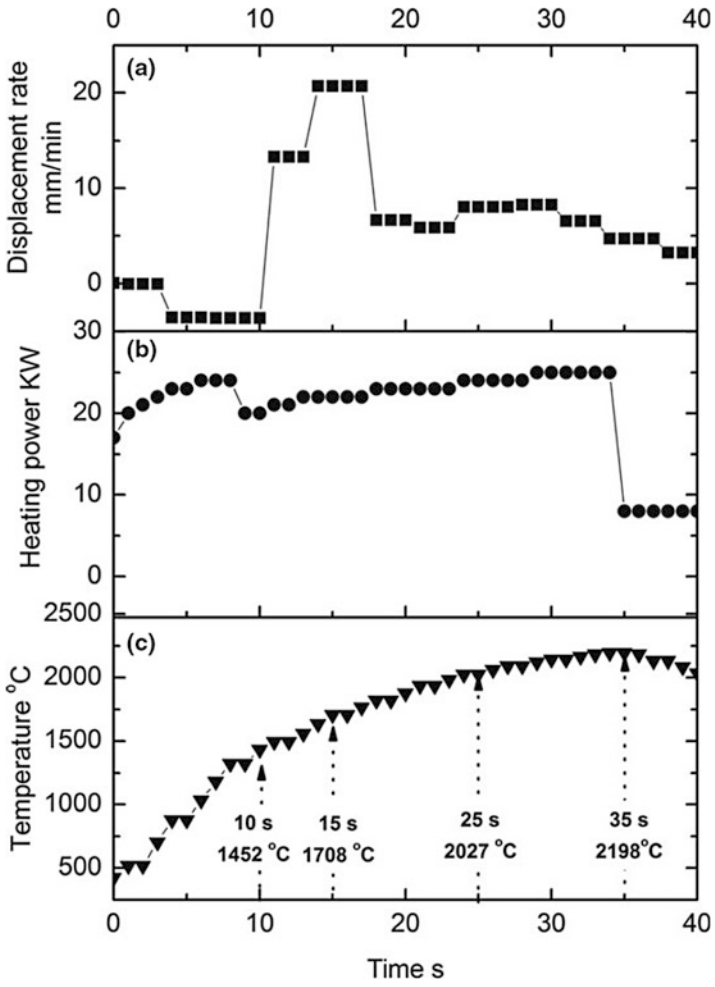

Fig. 5.9 Displacement rate (**a**), heating power (**b**), and temperature (**c**) during flash sintering of ZrB_2 (discharge time 35 s). (Reprinted from Grasso et al. [14], Copyright (2014) with permission of John Wiley & Sons)

less significant. A characteristic feature of the sintered specimens was a nonuniform density across the diameter of the pellet with the outer regions remaining porous (due to heat losses) and the core reaching nearly full density. An altered ratio of SiC observed by the authors is an evidence of thermal decomposition of silicon carbide (Fig. 5.13). From the known decomposition temperatures of SiC, it was possible to conclude that the sintered specimen experienced temperatures much higher than that of the furnace (1200 °C). The fact that the compacts heat treated before the flash sintering experiments showed a lower flash sintering temperature suggests that the initial formation of inter-particle contacts to form a continuous current pathway is

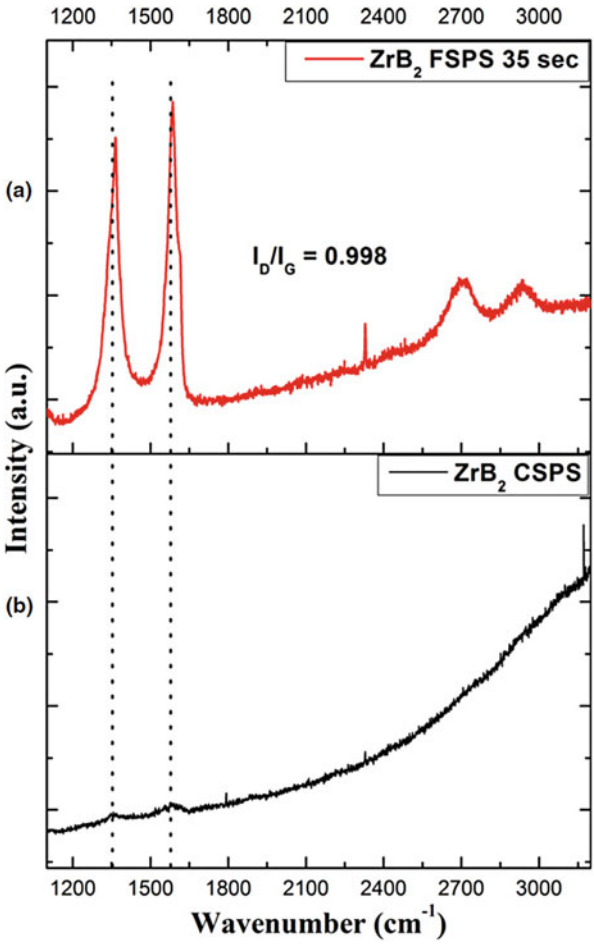

Fig. 5.10 Raman spectra of the ZrB_2-based compacts sintered from a powder containing 0.2 wt.% of carbon and 0.8 wt.% of oxygen: (**a**) flash sintering in a SPS chamber completed in 35 s, (**b**) conventional SPS. In the compact processed by SPS, the reaction between the remaining ZrO_2 and carbon is complete, and the carbon is removed in the form of CO. (Reprinted from Grasso et al. [14], Copyright (2014) with permission of John Wiley & Sons)

critical in determining the flash sintering temperature. According to the authors, the role of the sintering aids was also to establish better inter-particle contacts at low temperatures prior to flash sintering, while the main phenomenon responsible for the occurrence of flash sintering is Joule heating. It is noted that their flash sintering facility is similar to the SPS (induction heating of a graphite susceptor is used as a "furnace"; however, the sample is not in contact with it but insulated by alumina tubes) but differs from it by the absence of the die and by forcing the electric current through the sample, by means of which higher heating rates than in the SPS facilities can be achieved.

Olevsky et al. [15] proposed a modified flash sintering technique – flash hot pressing (or "flash spark plasma sintering") – in which pressure can be applied to the sample to stabilize the flash sintering process. Flash hot pressing can be conducted using conventional SPS facilities using a specially designed tooling. Alternatively, SPS facilities with hybrid heating can be used. The modified tooling included a

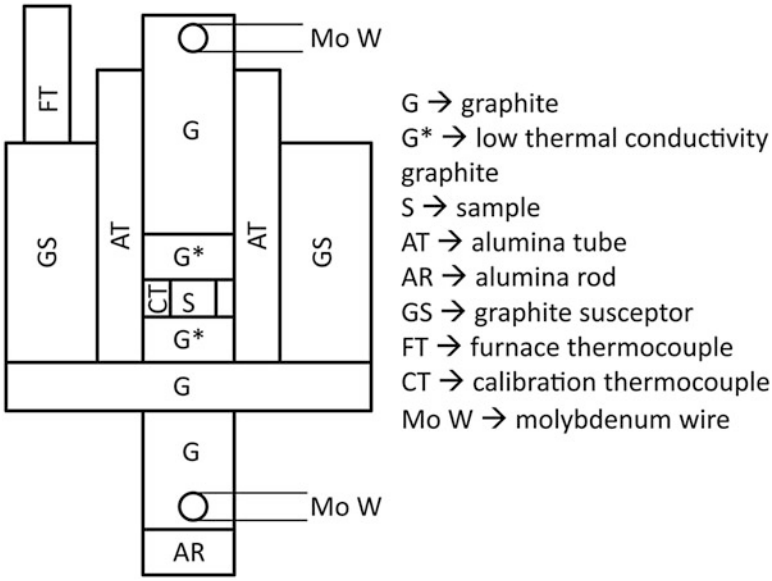

Fig. 5.11 Schematic of the flash sintering setup used in Ref. [12]. (Reprinted from Zapata-Solvas et al. [12], Copyright (2013) with permission from Elsevier)

copper collar tube, which acted as a heating element at temperatures below the melting point of copper (Fig. 5.14). At the initial stage of the process, the pre-sintered specimen is isolated from the electric current-carrying elements of the tooling and is, therefore, heated by radiation only. Once the melting point is reached, the tube collapses, so that the electrical contact between the punch and the tube is disrupted and the contact between the punch and the sample is established. The choice of copper as a material of the sacrificial collar was dictated by the fact that, at temperatures close to the melting point of copper, the major contribution to the overall electrical conductivity of SiC starts to come from its intrinsic conductivity, which increases exponentially with temperature above 1500 K. At temperatures below the melting point of copper, the conductivity of SiC has extrinsic nature and is determined by the presence of impurities. Flash hot pressing (flash spark plasma sintering) of a SiC powder allowed obtaining SiC compacts with a relative density of 99% without any noticeable grain growth (Fig. 5.15). The top edge of the sacrificial copper collar was exposed to the radiation thermometer, which was used by the SPS to regulate its temperature. Figure 5.16 shows the flash character of densification of the SiC pre-consolidated specimen: a spike in the temperature coincides with the spike in the relative density, while an increase in conductivity makes the SPS apparatus reduce the electric current.

The assembly designed for flash hot pressing has advantages of adding variable parameters to the flash sintering-based processing, which can be used to control the sintering efficiency. These parameters are the height of the copper collar and the applied pressure. Figure 5.17 shows the fracture surface of the compacts obtained using short and tall collars. In the case of a short collar, a relative density of 77% was

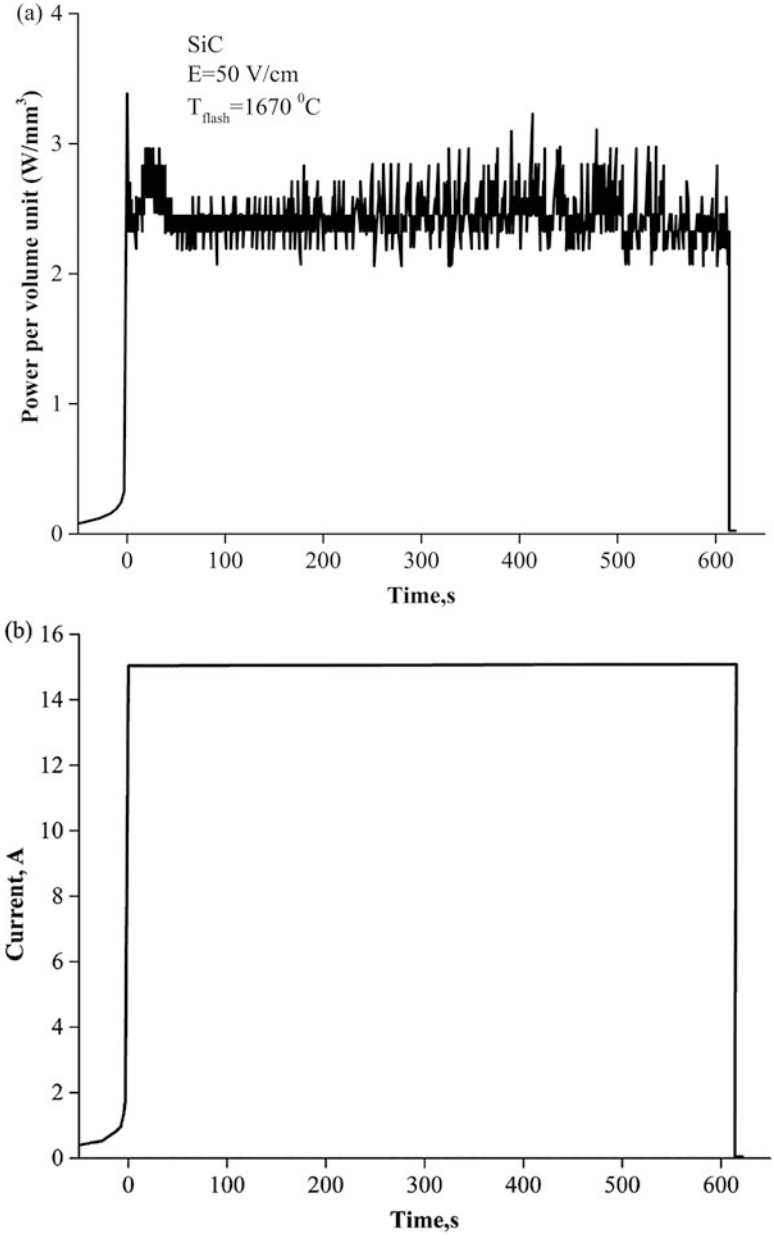

Fig. 5.12 Power per unit volume during flash sintering of SiC (**a**), SiC+(Al_2O_3 + Y_2O_3) (**c**), and SiC+ (Al + B_4C + C) (**d**); a sudden increase in current during sintering of SiC is shown in (**b**). (Reprinted from Zapata-Solvas et al. [12], Copyright (2013) with permission from Elsevier)

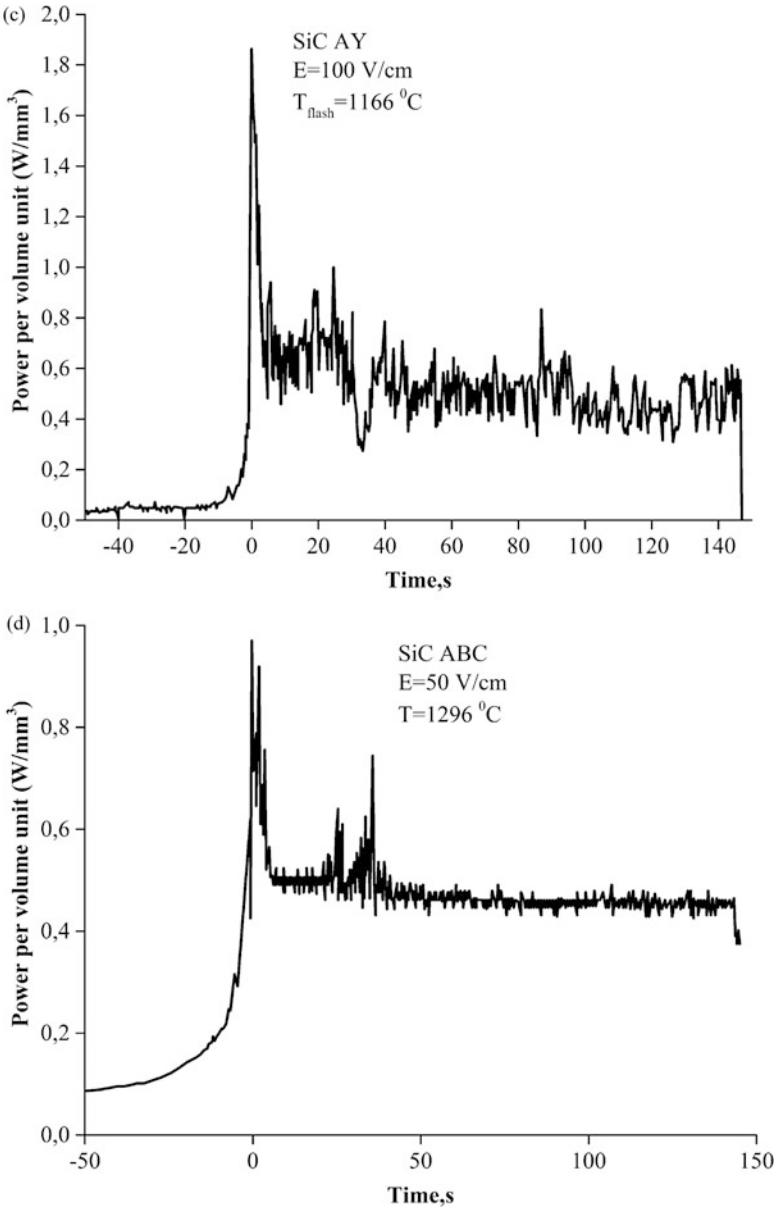

Fig. 5.12 (continued)

achieved, while the use of a long collar led to a higher relative density of 86%. Experiments with a punch with an oblique surface showed that by changing the applied pressure during flash hot pressing, the density of the sintered material can be varied. Figure 5.18 shows a SiC compact, in which zones with different values of shrinkage were formed corresponding to relative densities of 78% and 91%.

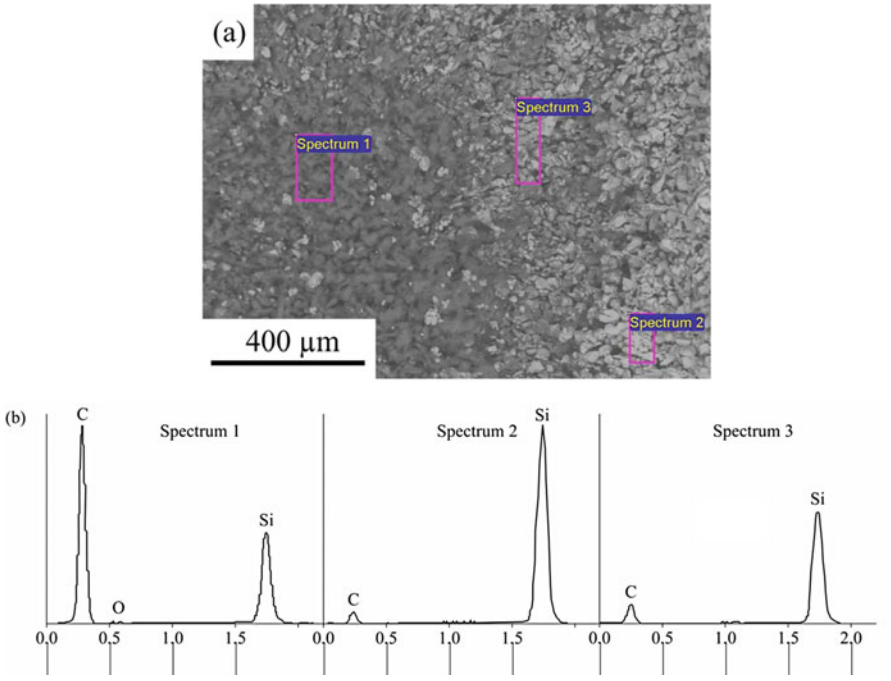

Fig. 5.13 SEM and EDX analyses of SiC flash sintered at 15 A and 200 $V \cdot cm^{-1}$. (Reprinted from Zapata-Solvas et al. [12], Copyright (2013) with permission from Elsevier)

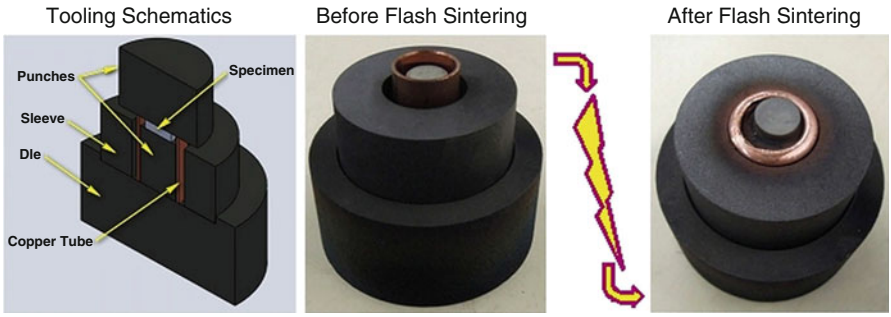

Fig. 5.14 Die design for flash hot pressing: a sacrificial copper collar is used as a supporting and a heating element for the pre-consolidated specimen at temperatures below the melting point of copper. (Reprinted from Olevsky et al. [15], Copyright (2015), Rights managed by Nature Publishing Group. This work is licensed under a Creative Commons Attribution License, http://creativecommons.org/licenses/by/4.0/)

The approach elaborated in Ref. [15] is different from die-free flash sintering of a pre-sintered pellet of an initially conductive material in a SPS facility between graphite punches by maximizing the power. In the die-free flash SPS [14], the ZrB_2 sample was preheated from the beginning of the process by the electric current

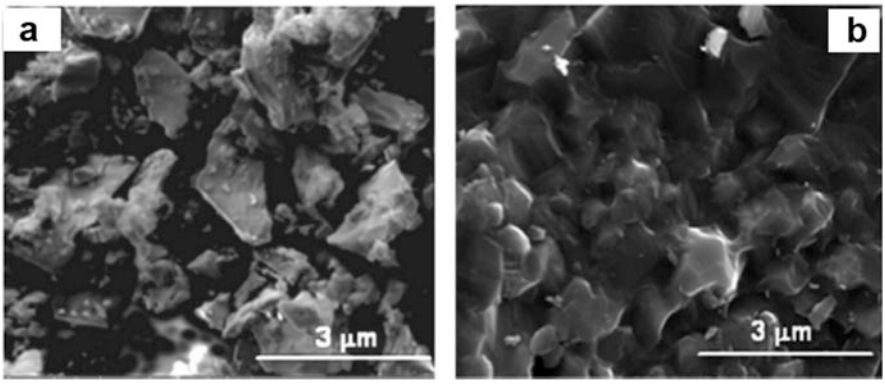

Fig. 5.15 The SiC powder (**a**) and the fracture surface of the compact (**b**) processed from this powder to a relative density of 99% by flash hot pressing (flash spark plasma sintering). (Reprinted from Olevsky et al. [15], Copyright (2015), Rights managed by Nature Publishing Group. This work is licensed under a Creative Commons Attribution License, http://creativecommons.org/licenses/by/4.0/)

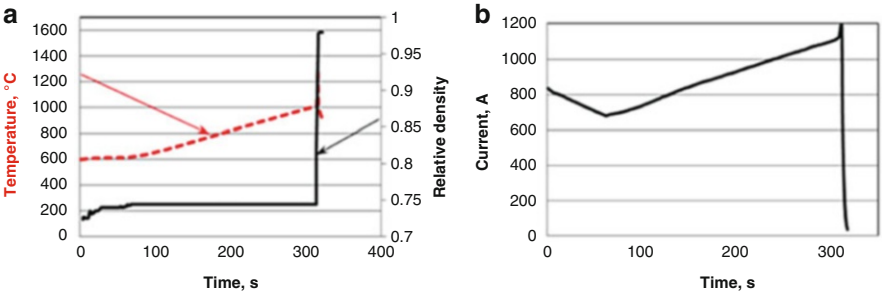

Fig. 5.16 (**a**) Temperature (dashed red line) and relative density (solid black line) of the SiC compact subjected to flash hot pressing, (**b**) evolution of electric current during flash hot pressing. (Reprinted from Olevsky et al. [15], Copyright (2015), Rights managed by Nature Publishing Group. This work is licensed under a Creative Commons Attribution License, http://creativecommons.org/licenses/by/4.0/)

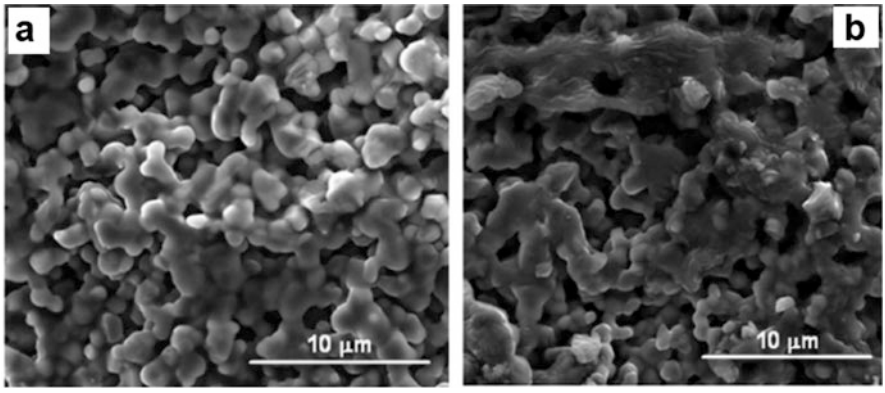

Fig. 5.17 Fracture surface of the SiC compacts consolidated by flash hot pressing (flash spark plasma sintering): (**a**) short copper collar (tube), (**b**) tall copper collar. (Reprinted from Olevsky et al. [15], Copyright (2015), Rights managed by Nature Publishing Group. This work is licensed under a Creative Commons Attribution License, http://creativecommons.org/licenses/by/4.0/)

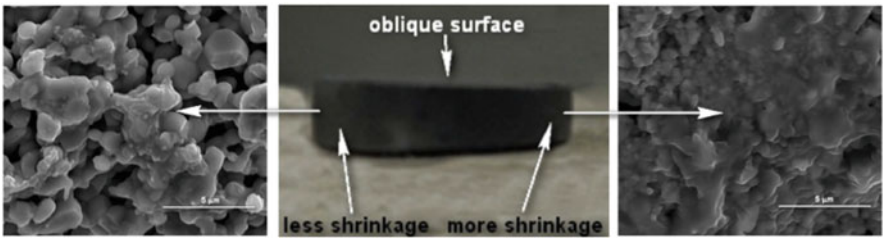

Fig. 5.18 Fracture surface and general view of the consolidated SiC compact processed by flash hot pressing using a punch with an oblique surface. (Reprinted from Olevsky et al. [15], Copyright (2015), Rights managed by Nature Publishing Group. This work is licensed under a Creative Commons Attribution License, http://creativecommons.org/licenses/by/4.0/)

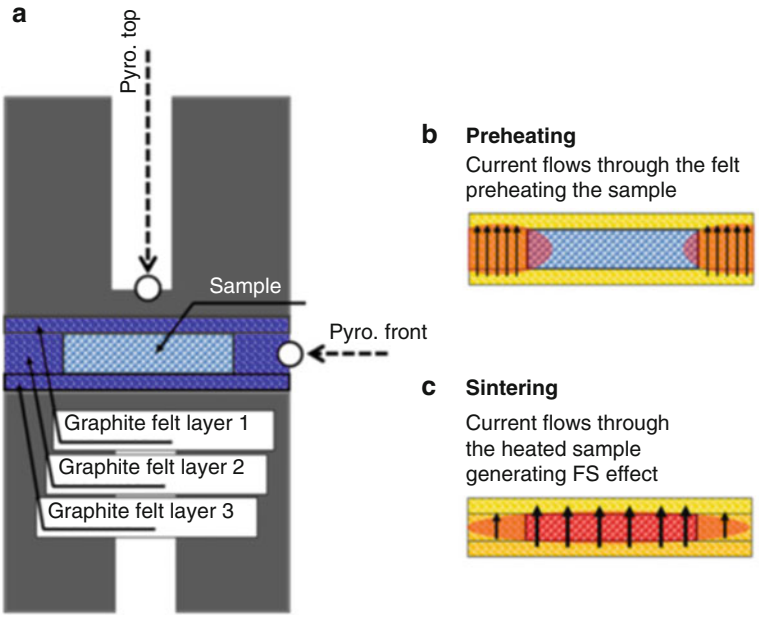

Fig. 5.19 Experimental setup for conducting flash SPS (**a**) and schemes showing the distribution of electric current at the preheating stage (**b**) and flash sintering stage (**c**). (Reprinted from Grasso et al. [16], Copyright (2016) Grasso et al., This is an open access article under the terms of the Creative Commons Attribution License, https://creativecommons.org/licenses/by/4.0/)

passing through it. Also, the use of a sacrificial copper collar makes the process presented in Ref. [15] different from the process, in which a graphite felt around the sample was used to establish conditions to preheat the pre-compacted SiC before flash sintering in a SPS facility [16, 17]. A schematic demonstrating the use of graphite felt as a conducting element at low temperatures, at which SiC is still too resistive, is shown in Fig. 5.19. At higher temperatures, the SiC compact is carrying the major fraction of the electric current.

5.2 Mechanisms of Flash Sintering

As flash sintering is usually conducted without the application of pressure, it presents a field-assisted sintering method, which allows studying the effect of electric current per se on densification and grain growth without having to overcome the difficulties of separating the sintering enhancement effects induced by pressure from those related to the passing current [18]. Raj [4] suggests that Joule heating, though involved in the process, cannot explain the phenomenon, as the increased temperature of the sintered material is still several hundred degrees lower than that required for such a fast sintering according to the calculations based on the Arrhenius equation. The conductivity of the oxide materials taken for the studies is electronic, and they behave as semiconductors upon heating. Initially, a constant voltage is applied to the compact (Fig. 5.20). A rapid increase in conductivity causes a surge in the powder dissipation. The power supply is then switched to the current control (Fig. 5.21) [4, 25]. The difficulty in explaining the flash sintering effect is, therefore, due to the fact that the conductivity and densification are dependent on different moving species — electrons and ions, respectively. Raj [4] believes that more attention should be directed to the mechanism of the field influence on densification during flash sintering, as the electric field can produce an avalanche of Frenkel pairs

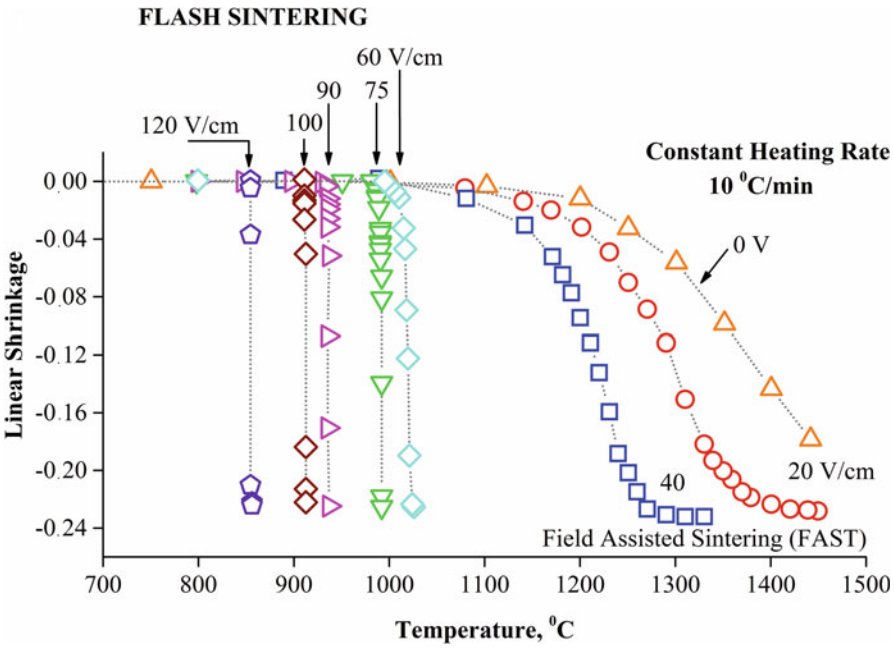

Fig. 5.20 Shrinkage rates of yttria-stabilized zirconia (3YSZ) under an applied field. The instability observed at a field strength of 40 $V \cdot m^{-1}$ leads to sintering in a few seconds. (Reprinted from Cologna et al. [2], Copyright (2010) with permission John Wiley & Sons)

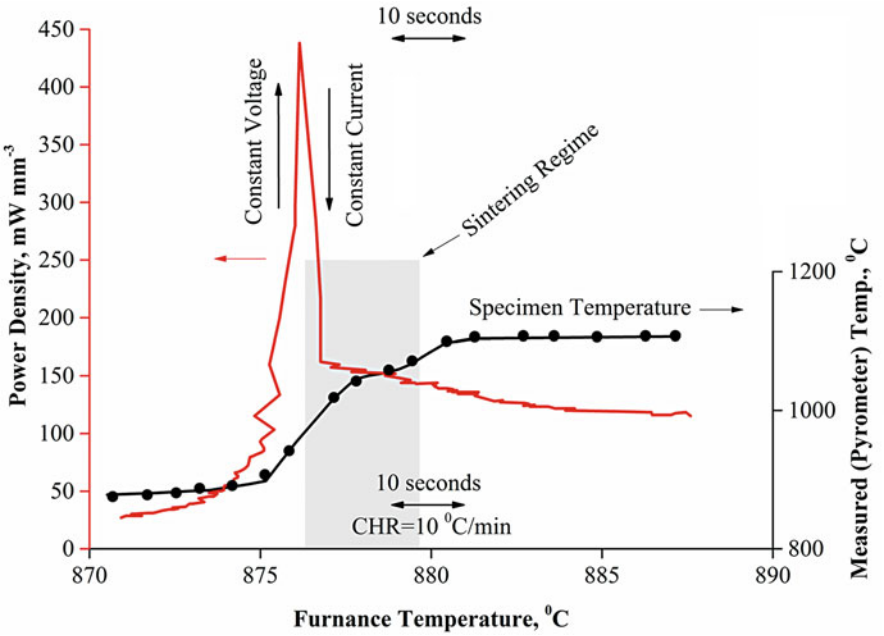

Fig. 5.21 The power density and the specimen temperature during a flash sinter-forging experiment. (Reprinted from Raj [4], Copyright (2012) with permission from Elsevier)

and induce their ionization [26]. An increased concentration of Frenkel pairs would facilitate mass transport in the sintered material.

For initially non-conducting $SrTiO_3$, higher compact densities were achieved at lower applied fields, as was reported by Karakuscu et al. [27], similar to the results presented in Ref. [24]. At an applied field of 1000 $V \cdot m^{-1}$, flash sintering started at 740 °C, but the final sintered density was below 70%. At 500 $V \cdot m^{-1}$, flash sintering occurred at 900 °C yielding a compact 76% dense. A weaker field of 150 $V \cdot m^{-1}$ induced flash sintering at 1200 °C, which was closer to a field-assisted process as the densification was not instantaneous (Fig. 5.22). The microstructure of the sintered compact shown in Fig. 5.23 indicates significant grain growth in the sample sintered at 1200 °C relative to that sintered at 900 °C. The ability of the $SrTiO_3$ phase to be flash sintered was attributed to an increase in its conductivity during flash sintering through the introduction of defects associated with nonstoichiometric phases. This conclusion was supported by the characterization results of the flash-sintered material by transmission electron microscopy, X-ray diffraction, and photoinduced reflectivity dynamics, which all indicated higher content of defects in the sintered material relative to the powder. Future investigations of the defect structures in the materials will shed light on the processes occurring during flash sintering and contribute to a deeper understanding of its mechanisms.

Grasso et al. [28] analyzed the temperature distribution in an yttria-stabilized zirconia dog bone-shaped compact (Fig. 5.24) under conditions of flash sintering by

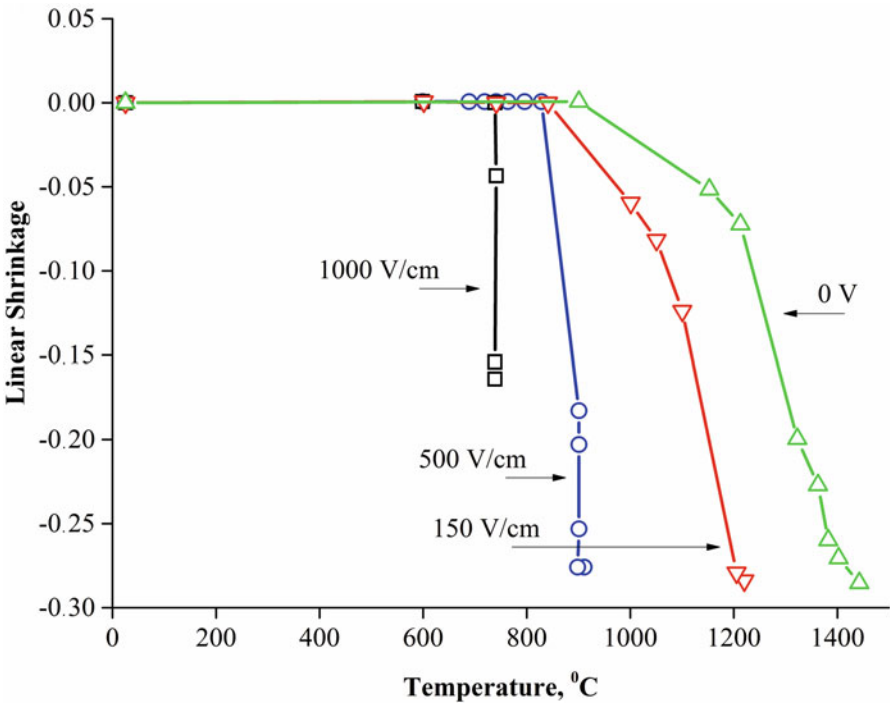

Fig. 5.22 Linear shrinkage of $SrTiO_3$ at different applied electrical fields versus furnace temperature (heating rate 10 °C·min^{-1}). (Reprinted from Karakuscu et al. [27], Copyright (2012) with permission of John Wiley & Sons)

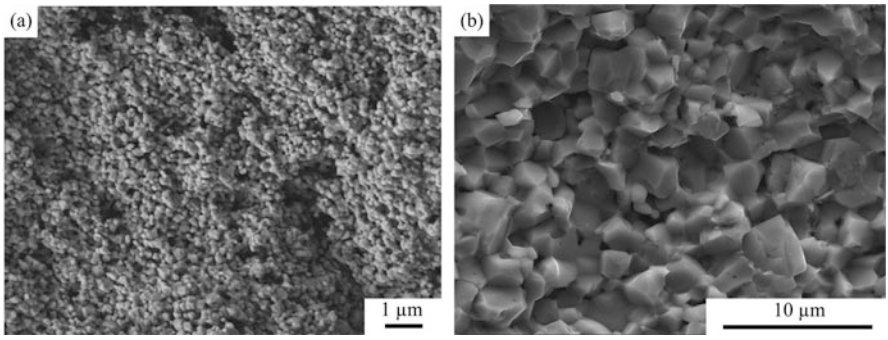

Fig. 5.23 SEM images of the flash-sintered $SrTiO_3$: (**a**) 500 V·cm^{-1}, 60 mA, flash sintering occurred at 900 °C; (**b**) 150 V·cm^{-1}, 500 mA, flash sintering occurred at 1200 °C. (Reprinted from Karakuscu et al. [27], Copyright (2012) with permission of John Wiley & Sons)

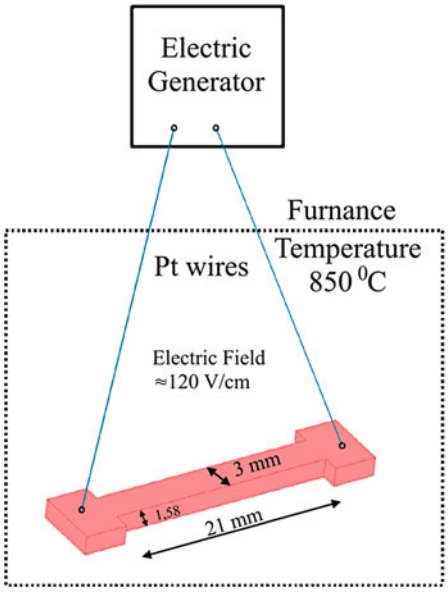

Fig. 5.24 A dog bone-shaped specimen used in flash sintering. (Reprinted from Grasso et al. [28], Copyright (2011) with permission from the Ceramic Society of Japan)

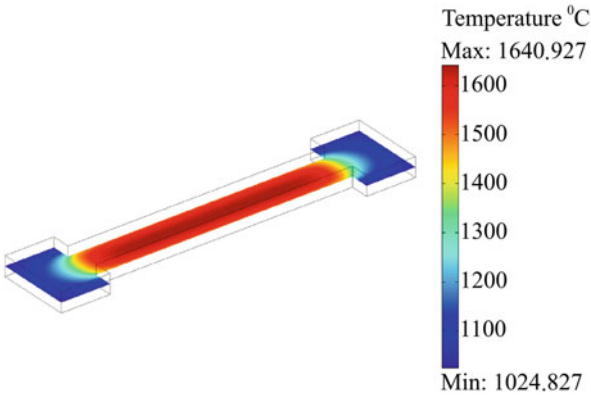

Fig. 5.25 Finite element model simulation of the temperature distribution in the yttria-stabilized zirconia dog-bone shaped compact under a power of 70 W applied for 3 s. A field intensity of 120 V·cm^{-1} was applied when a furnace temperature reached 850 °C. (Reprinted from Grasso et al. [28], Copyright (2011) with permission from the Ceramic Society of Japan)

means of finite element model simulation and conducted flash sintering experiments with doped and undoped zirconia. In the simulation, the electrical and thermal conductivities of the material as well as its heat capacity were assumed to depend on the temperature. The simulation results showed that the flash sintering phenomena should be ascribed to a sudden temperature increase inside the sample. As is seen from Fig. 5.25, the temperature rises very rapidly – from 850 to 1600 °C.

By comparing the microstructure of the tetragonal yttria-stabilized zirconia and undoped zirconia compacts after the flash sintering experiments, it was found that the former was well sintered, while the latter was still porous, which indicated the primary significance of the electrical conductivity of the material in the success of

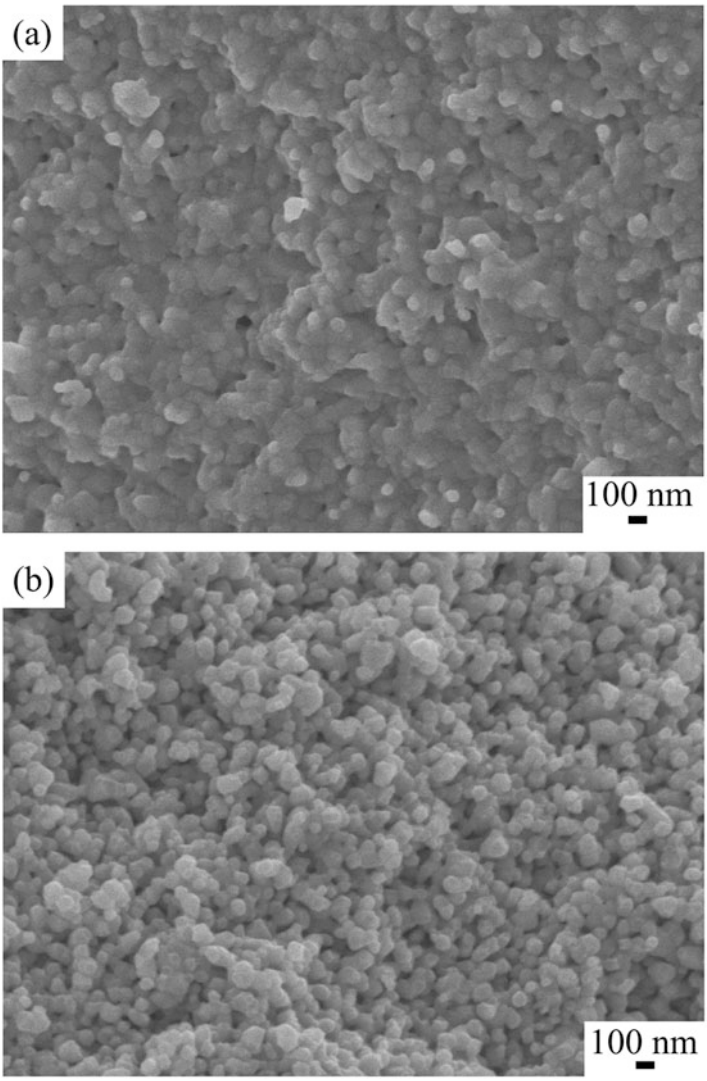

Fig. 5.26 Fracture surface of tetragonal yttria-stabilized zirconia (**a**) and undoped zirconia (**b**) subjected to flash sintering (120 $V \cdot cm^{-1}$ applied when the furnace temperature reached 850 °C). (Reprinted from Grasso et al. [28], Copyright (2011) with permission from the Ceramic Society of Japan)

the flash sintering process (Fig. 5.26). Grasso et al. [28] emphasized the significance of the flash sintering technique as an energy-saving method due to the utilization of highly localized heating and short processing times.

Using AC impedance spectroscopy, Park and Chen [29] performed in situ thermometry and measured temperatures exceeding 1500 °C reached within a few

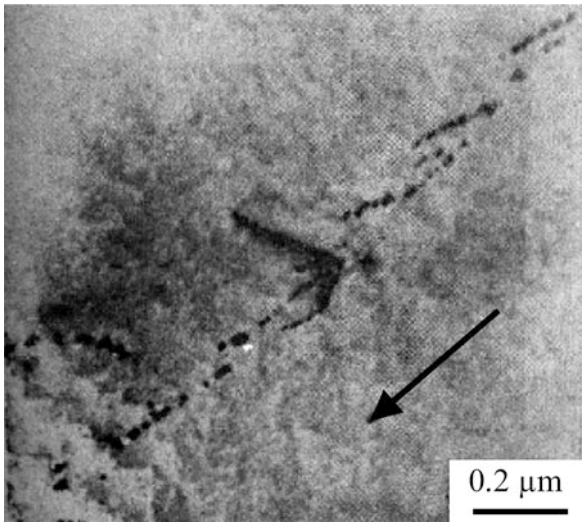

Fig. 5.27 Bright-field electron micrograph of a MgO crystal showing precipitates near a sub-grain boundary. (Reprinted from Narayan [31], Copyright (2013) Acta Materialia Inc., with permission from Elsevier)

seconds in 8 mol.% yttria-stabilized zirconia disks 0.25–0.65 mm thick heated in a furnace at a field intensity of 16 $V \cdot mm^{-1}$. They found that the temperature runaway was more pronounced in samples with smaller surface-to-volume ratio. Todd et al. [30] showed that the main electrical and thermal characteristics of flash sintering of 3YSZ can be predicted accurately through the inverse Arrhenius dependence of resistivity and concluded that they are a classic consequence of the negative temperature coefficient of resistivity leading to runaway Joule heating at a constant voltage.

Narayan [31] explained electric field-induced phenomena, such as flash sintering, reduction in the flow stress, and hindered grain growth by a unified mechanism, which includes defect segregation at dislocations and grain boundaries and their selective Joule heating. The segregation effects in applied fields have been observed experimentally. Figure 5.27 shows precipitates with an average size of 10 nm near a sub-grain boundary of a MgO crystal treated in an electric field. The segregation effects were observed only in the samples treated in electric field; further annealing of the crystal without field results in the disappearance of the segregation effects.

Impurities with higher cationic valencies compared with the host atoms increase the electron trapping and generation of defects. The segregation of defects at grain boundaries causes reverse vacancy jumps and slows down the grain growth rate. The segregation effects increase the ionic and electronic transport along the grain boundaries. The AC field was found to be more effective in causing segregation compared with the DC field under similar parameters [31]. These effects in metals are less pronounced because of their higher thermal diffusivity and lower localization of heat compared with ceramics. At high electric fields, ionic and electronic conduction lead to an avalanche, where grain boundaries are selectively heated to melting. Flash sintering of ceramics can thus be understood as a consequence of selective melting of grain boundaries. The enhancement of conductivity with increasing temperature is

an avalanche effect in an uncontrolled state and can lead to melting and evaporation of the material between the electrodes. In practice, the current flow is limited to control the process. Narayan argues that Joule heating of the grain boundaries and not of the whole volume of the material should be considered. While in the solid state Joule heating cannot account for high sintering rates observed in flash sintering [26], it can explain the observed heating rates in the presence of liquid phases with high diffusivities (10^{-4}–10^{-5} cm^2 s^{-1}).

Fast volumetric heating leading to flash sintering of a porous compact can also be realized by microwave heating. Flash sintering occurs when the processing conditions are such that facilitate the development of thermal runaway. Bykov et al. [32, 33] suggested that grain boundaries play a key role in the flash sintering process being the regions of high concentrations of defects and impurities. The localized preferential absorption of microwave radiation by the grain boundaries results in the grain-boundary softening or premelting. Thanks to softening, rapid densification of the granular medium having reduced viscosity-grain boundaries can occur via rotation and sliding of the grains, which accommodate their shape by means of fast mass transport through the liquid or quasi-liquid phase. It was shown that the heating rate (the absorbed power) greatly influences the microstructure (Fig. 5.28).

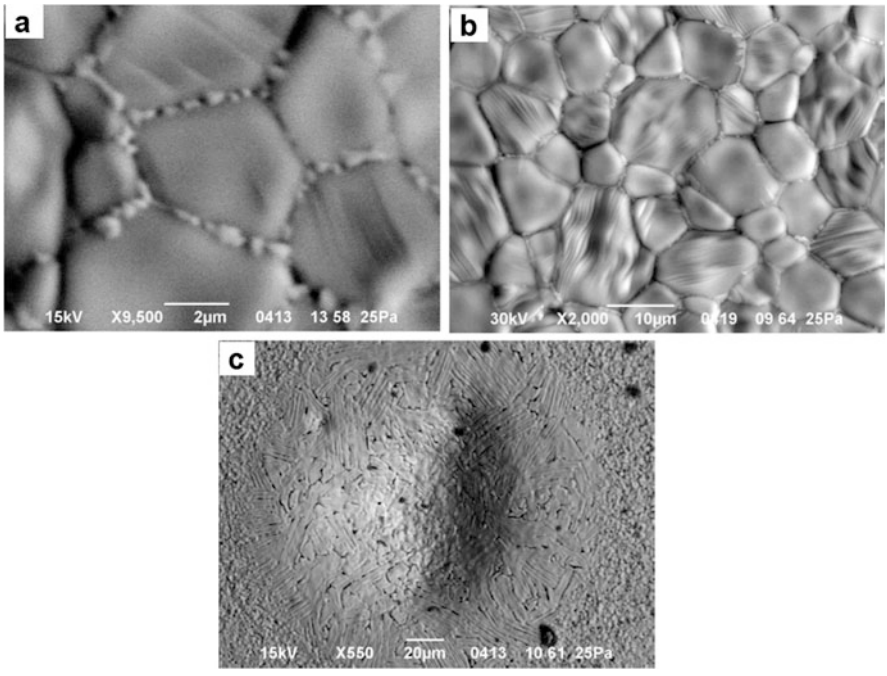

Fig. 5.28 Microstructure of the Yb:$(LaY)_2O_3$ ceramics flash sintered by microwave heating: (**a**) heating at 50 °C·min^{-1} up to 1500 °C, (**b**) heating at 100 °C·min^{-1} up to 1500 °C, (**c**) heating at 7000 °C·min^{-1} up to 1580 °C. (Reprinted from Bykov et al. [32], Copyright (2016) Bykov et al. This article is an open access article distributed under the terms and conditions of the Creative Commons Attribution License http://creativecommons.org/licenses/by/4.0/)

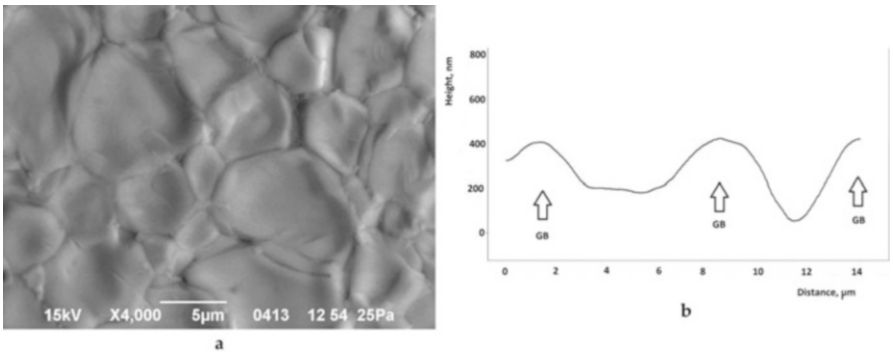

Fig. 5.29 A SEM image of the surface of the sintered Yb:$(LaY)_2O_3$ ceramics flash sintered by microwave heating at 200 °C·min^{-1} up to 1500 °C (**a**), atomic force microscopy profiles of the adjacent grains (**b**). (Reprinted from Bykov et al. [32], Copyright (2016) Bykov et al. This article is an open access article distributed under the terms and conditions of the Creative Commons Attribution License (http://creativecommons.org/licenses/by/4.0/)

At a heating rate of 50 °C·min^{-1}, the grain boundaries showed frozen droplets. At a higher heating rate (100 °C·min^{-1}), these droplets merged and formed grain-boundary layers, which showed a different contrast in comparison with the body of the grains in back-scattered electron microscopy images. At a much higher heating rate (7000 °C·min^{-1}), the regions that experienced melting were larger still being localized.

Bykov et al. [32] analyzed the structure of the specimen's surface and its profile using a combination of scanning electron microscopy and atomic force microscopy. As can be seen in Fig. 5.29, the relief of the sintered compact is uneven, with edges of the grains protruding from the surface. The protruding areas form due to a larger specific volume of the material in the molten state relative to that in the solid state. It was suggested that the molten part of the material fills the triple points of the granular structure and is partially extruded to the surface. The premelting of the particle surface can occur well below the melting point of the bulk material. The elemental analysis of the grains and the intergranular phase in flash-sintered Yb:$(LaY)_2O_3$ showed that the intergranular phase is La- and O-enriched and Y-depleted.

According to Chaim [34], the main problems that make it difficult to investigate the flash sintering mechanisms include the uncertainty of the real temperature at the contacts between the particles (which is difficult to measure, while estimations may vary by hundreds of degrees), the assumption of uniform sintering throughout the specimen volume, and the assumption of the solid-state nature of the flash events. Chaim proposed a model for rapid densification of flash-sintered ceramics [34]. In this model, a liquid film forms by local melting at the inter-particle contacts due to preferred Joule heating followed by thermal runaway. Local densification occurs via particle rearrangement enabled by spreading of the liquid due to local attractive capillary forces. The contacts melt in a random hierarchical manner. The rapid densification is aided by the local increase in the specific volume. The volume densification is closely connected with the percolation effect: at the percolation

threshold, a sudden increase in the electrical conductivity and dissipated power is related to the percolation of current through the softened part of the sintered material or liquid [35]. The invasive nature of the melt at the contacts leads to the formation of an advancing front, which forms the percolative pass for the current flow (liquid "circuit"). In composite (multiphase systems), flash events can involve a particular phase. In this regard, study by Candelario et al. [36] should be mentioned, who used yttrium aluminum garnet $Y_3Al_5O_{12}$ (YAG) as a sintering additive in flash sintering of a SiC powder. The YAG additive melted and promoted liquid phase-assisted densification.

A promising approach to studying the flash sintering mechanisms is in situ diffractometry using synchrotron radiation, which allows gaining information on the fast structural changes occurring in the material during the flash sintering process. Reversible transformations (dependent on the presence of electric field) – the formation of new phases and texturing – have been reported [37, 38]. Figure 5.30 shows evidence of a reversible transformation in titania induced by the application of

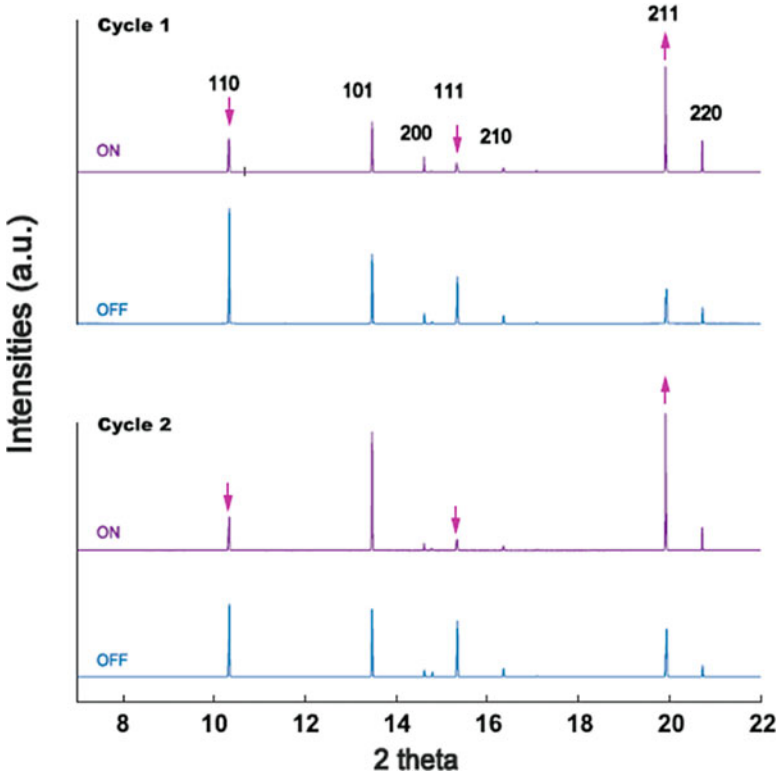

Fig. 5.30 X-ray diffraction patterns of titania compacts experiencing two cycles of a constant flash state under current control: the relative intensities of (211), (110), and (111) reflections change when the electric current is applied relative to the state without applied current. (Reprinted from Jha et al. [38], Copyright (2015) with permission from Elsevier)

electric current. The specimen temperature was measured to be 925 °C using a platinum standard [38]. It was proven that Joule heating was not the cause of the observed changes in the relative intensities of the peaks, as heating of the specimens up to 900–1000 °C without electric field did not lead to any such changes in the diffraction patterns.

McWilliams et al. [18] have reported an unusual phenomenon – the flash sintering behavior of Al alloy AA5083. Upon reaching a certain temperature, the compact consolidated from the alloy powder turned from an insulating state into a conducting state. It was shown that Joule heating alone cannot account for the observed flash sintering behavior. The authors suggested that the dielectric breakdown of the surface oxides present on the powder particles played a significant role in determining the ability of the powder compact to densify in the flash manner. Flash sintering behavior of metallic powders was also observed during processing of polymer/silver mixtures under antenna microwave illumination allowing fast agglomeration and consolidation of silver particles (microwave flash sintering) [39, 40].

An original metal powder flash sintering method using microwaves was elaborated in Ref. [41]. An unusually fast (60 s) thermal and sintering runaway of a Ti-6Al-4V powder was experimentally observed under microwave illumination. The experimental results were compared with the outcomes of the electromagnetic–thermal–mechanical simulation, which is able to predict the cavity microwave distribution, heating, sample densification, and shape distortions. The developed multiphysics model revealed that the specimen's runaway does not result from the intrinsic properties of the sintered material properties but is caused by the resonance phenomenon thermally activated by the surrounding tooling material. In the experiments, a partially densified compact (relative density 40%) was surrounded by a SiC nanopowder. The sample thermal runway was the result of the combination of multiple factors including the resonance phenomenon, the location of the sample in a high magnetic field area, and the confinement of the heat generated in the sample by the nano-SiC powder. The originality of this microwave flash sintering approach is in the presence of a metal thermal runaway that does not originate from the metal properties. The comparison of the microwave and conventional sintering kinetics indicated acceleration of the sintering behavior under microwave heating. The developed microwave flash sintering does not require preheating in a furnace or electric connections (the process is contactless) and can be used for metals and alloys.

Local Joule heating and melting of the inter-particle contacts was suggested as an explanation of a peculiar microstructure development of $Mg_{2.1}Si_{0.487}Sn_{0.5}Sb_{0.01}$ under conditions of flash SPS [42]. A high initial conductivity of the material allowed direct Joule heating of the pre-compacted specimen in an assembly without a die or conductive wrap by pulsed current generated in a SPS facility (Fig. 5.31). The microstructures of the specimen sintered by conventional SPS (sintering in a die with and without a pre-sintering stage) and that obtained by flash SPS conducted without a die differ from each other. Specimens sintered by the SPS in a die were heated at a rate of 100 °C·min^{-1} to 750 °C; the specimen consolidated from the powder directly was held at the maximum temperature for 1 min, while there was no

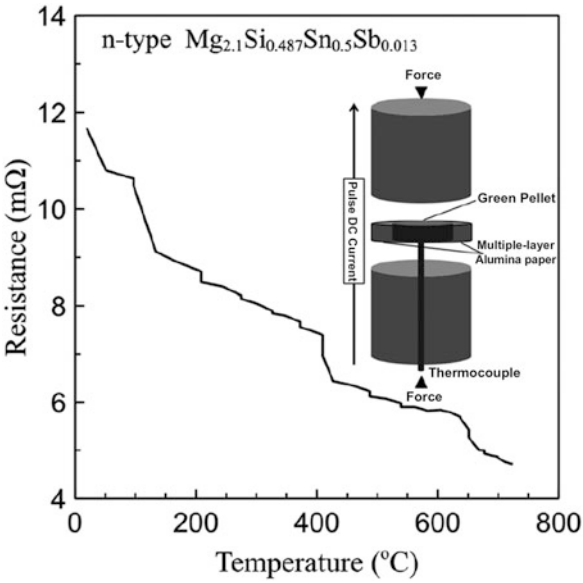

Fig. 5.31 Schematic of an assembly for flash sintering (no die or conductive wrap around the specimen is used, alumina paper covers the cylindrical surface of the specimen to reduce the radiation heat losses) and the resistance change of $Mg_{2.1}Si_{0.487}Sn_{0.5}Sb_{0.013}$ with the temperature during flash sintering under pulsed current in a SPS facility. (Reproduced from Du et al. [42]. This article is licensed under a Creative Commons Attribution 3.0 Unported Licence. https://creativecommons.org/licenses/by/3.0/)

holding at the maximum temperature in the experiment with the pre-sintered compact. The material sintered from the powder by conventional SPS showed no phase separation (Fig. 5.32a). In the material, processed twice by the conventional SPS (Fig. 5.32b), there was mild phase separation: solid solutions with different concentrations formed. The most interesting observation was made when the microstructure of the flash-sintered material was analyzed: a tin-enriched network formed through the microstructure, also engulfing magnesia (MgO) particles present on the surface of the agglomerates of the initial powder (Fig. 5.32c–d). Consequently, during flash sintering, changes in the microstructure, phase composition, and local chemical composition of the material can occur caused by local melting at the particle contacts.

Similar observations in terms of redistribution of elements in solid solutions were made by Corapcioglu et al. [43], who flash sintered $K_{0.5}Na_{0.5}NbO_3$ at 990 °C and 250 $V \cdot cm^{-1}$ for 30 s and found that the distributions of Na and K were not homogeneous. Rather, the distribution resembled a core–shell structure, in which the shell was K-rich and the core was Na-rich. The powder used for sintering did not show any core–shell compositional features. The compositional variations between the shell and the core were explained by grain-boundary melting during flash sintering followed by recrystallization upon cooling. When a flash-sintered sample was heat treated at 1000 °C for 4 h, the core–shell morphology disappeared. So, conventional heat treatment made potassium ions diffuse into the core and sodium ions diffuse from the core to the shell so that the equilibrium stoichiometry of $K_{0.5}Na_{0.5}NbO_3$ was restored.

For porous pre-sintered α-Al_2O_3 subjected to flash sintering at field strengths of 500–1500 $V \cdot cm^{-1}$, analogies between flash sintering and dielectric breakdown were

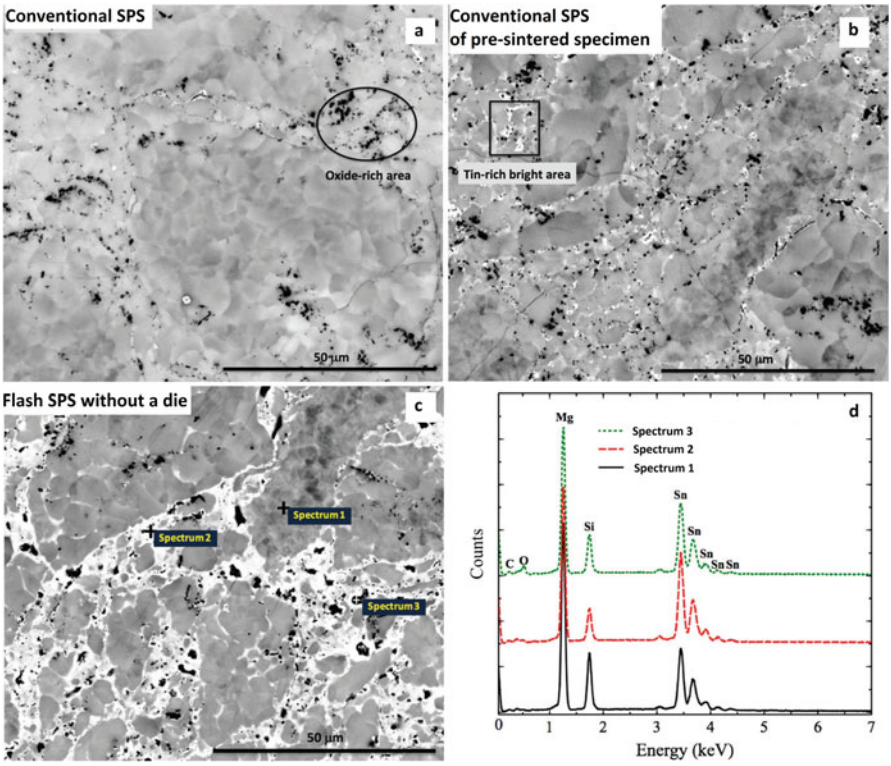

Fig. 5.32 Microstructure of the sintered $Mg_{2.1}Si_{0.487}Sn_{0.5}Sb_{0.013}$ (**a**–**c**) and spectra (**d**) taken from different points of (**c**); (**a**) conventional SPS from the powder, 750 °C, (**b**) conventional SPS of a pre-sintered compact, 750 °C, (**c**) flash SPS without a die, heating up to 700 °C at 1000 °C·min^{-1}. (Reproduced from Du et al. [42], This article is licensed under a Creative Commons Attribution 3.0 Unported Licence. https://creativecommons.org/licenses/by/3.0/)

found [44]. The authors suggest that elevated temperatures and sample porosity lead to a decrease in the breakdown strength down to values comparable to those at which flash events were observed. The processes of flash sintering and dielectric breakdown were found to be similar in terms of runaway and conductivity evolution. The incubation for flash sintering was compared to the pre-breakdown phenomenon. The relation between the incubation time and the pre-sintering temperature (porosity of the pre-sintered compact) showed that samples with a higher porosity require shorter incubation times. The electrical conductivity of the fully dense samples did not depend on the field strength, while that of the porous samples increased with increasing field strength. Fully dense α-Al_2O_3 materials did not show a flash behavior.

5.3 Materials Densified by Flash Sintering

In SPS, the sintering times are quite short – the total duration of the process is usually from several minutes to several tens of minutes. It is technologically attractive to further shorten the sintering process and reduce the sintering times down to several seconds and increase the energy efficiency of sintering. The greatest limitation of the initially proposed flash sintering approaches is the lack of applicability of flash sintering to a wide range of materials. This limitation has been overcome by Manière et al. [45], who combined SPS and a flash sintering approach and developed a flash (ultra-rapid) spark plasma sintering method (net-shape flash SPS – NSFSPS) applicable to various materials regardless of their electrical resistivity. Powders of metals and insulating ceramics were consolidated to produce compacts with a homogeneous microstructure within sintering times of 8–35 s. Extraordinary fast and homogeneous heating was concentrated in the sample's volume and punches. The controllable flash phenomenon was enabled by the combination of the electric current concentration around the sample and the confinement of the heat generated in this area by the lateral thermal contact resistance (TCR). The NSFSPS approach uses a graphite die electrically insulated by a sprayed boron nitride (BN) layer to concentrate the electric current into the sample, if electrically conductive, or in the nearby graphite foil, if electrically insulating (Fig. 5.33). The graphite die allows an easy control of

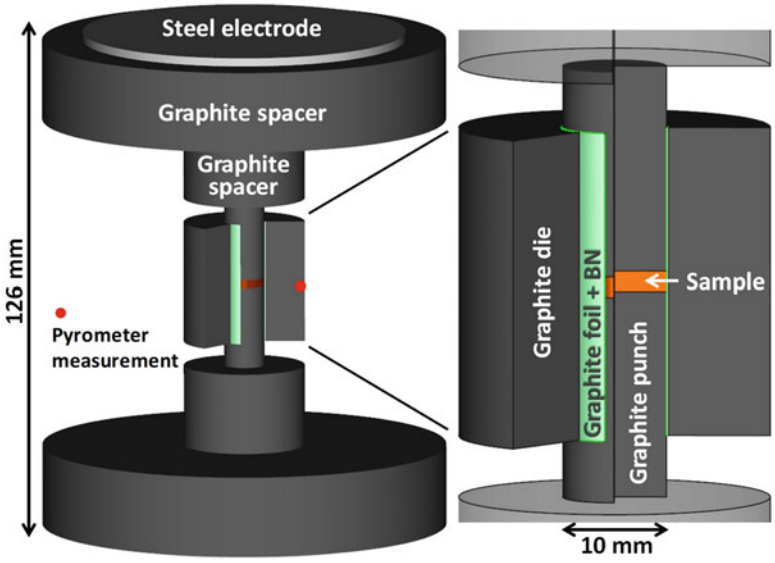

Fig. 5.33 Net-shape flash spark plasma sintering configuration. In order to concentrate the electric current on the sample area, the inner die surface is coated by an electrically insulating boron nitride (BN) spray. (Reprinted from Manière et al. [45], Copyright (2017), Rights managed by Nature Publishing Group. This work is licensed under a Creative Commons Attribution License, http://creativecommons.org/licenses/by/4.0/)

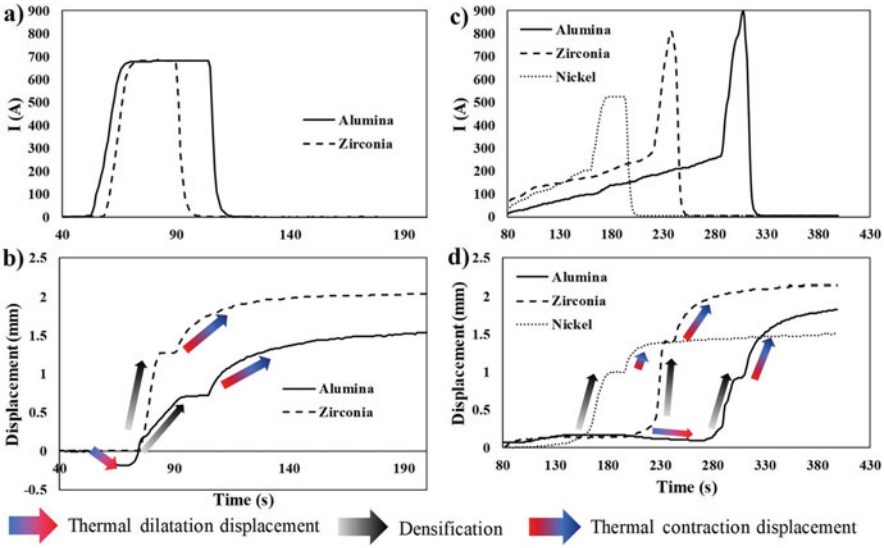

Fig. 5.34 Experimental electric current (**a**, **c**) and displacement (**b**, **d**) curves under constant current mode (**a**–**b**) and forced mode (**c**–**d**). (Reprinted from Manière et al. [45], Copyright (2017), Rights managed by Nature Publishing Group. This work is licensed under a Creative Commons Attribution License, http://creativecommons.org/licenses/by/4.0/)

the final shape of the specimen and makes the overall pressure-assisted process more stable. The NSFSPS approach uses graphite tools for high-temperature applications and good thermal shock resistance. This approach is related to the current concentration method described in Ref. [46] but uses electric current patterns different from those of Ref. [46]. Using the NSFSPS approach, nickel, alumina, and yttria-stabilized zirconia powders were sintered in the flash mode [45].

The current cycle was imposed manually in two patterns: constant current mode and forced current mode (Fig. 5.34). In both the "constant current mode" and the "forced mode," the sintering time is shorter than 60 s. An electric current cycle with a forced runaway was realized by manually increasing the current at 70 $A \cdot min^{-1}$ up to the beginning of densification and at 2500 $A \cdot min^{-1}$ further up until the displacement plateau indicating the end of densification was reached. For nickel and alumina, the thermal runaway that appears in traditional flash sintering dealing with materials whose electrical conductivity increases with temperature was artificially imposed by the electric current pattern that reproduced a similar sample's thermal response.

Samples, the fracture surfaces of which are shown in Fig. 5.35, were nearly dense with a residual porosity between 1 and 3% for the ceramic samples and 5% for nickel. For zirconia and alumina, the grain size increased from 37–100 nm to 20 μm in about 10 s. This suggests that fast densification was accompanied by unusually fast grain growth. The comparison of the center/edge images reveals no obvious microstructural differences indicating a very homogeneous process. However, a

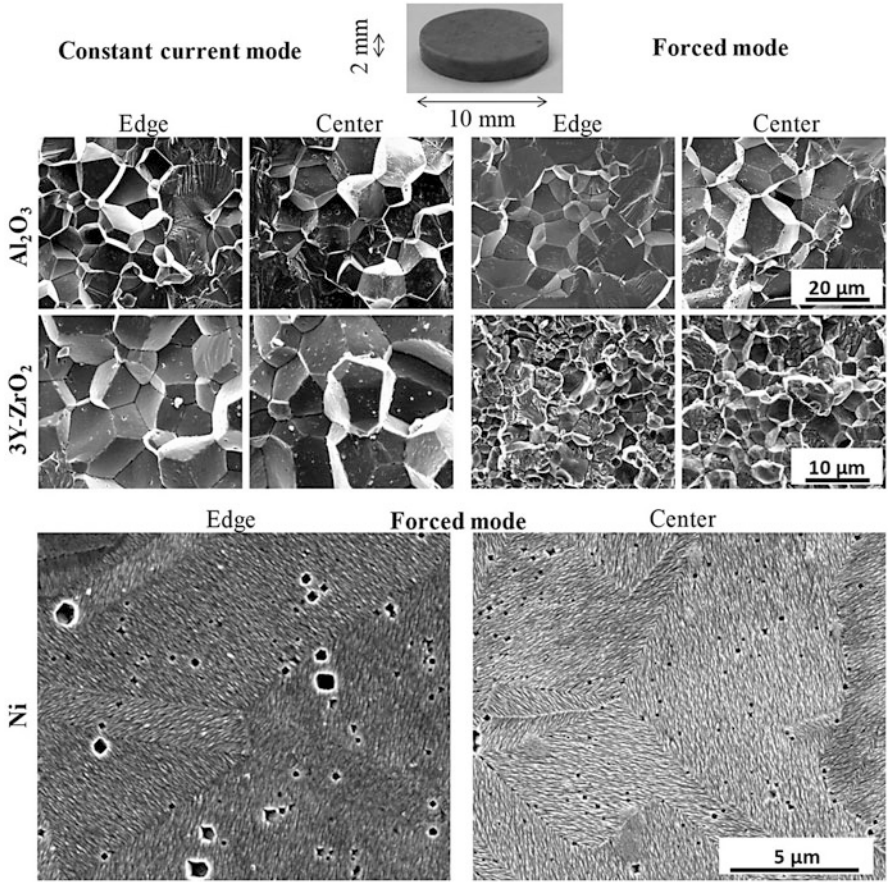

Fig. 5.35 SEM images in the centers and edges of nickel, zirconia, and alumina samples for constant and forced current modes. (Reprinted from Manière et al. [45], Copyright (2017), Rights managed by Nature Publishing Group. This work is licensed under a Creative Commons Attribution License, http://creativecommons.org/licenses/by/4.0/)

noticeable microstructure difference can be seen between the "constant current" mode and the "forced" mode in the zirconia samples. Zirconia becomes electrically conductive at high temperatures and seems to generate some heating instabilities (internal sample temperature runaway and overheating in the sample's area) which cause fast grain growth under the "constant current" mode. In comparison, the alumina sample that possesses a low electrical conductivity at low and high temperatures exhibits nearly no microstructure differences between the two modes. It appears that materials, which are normally impossible to flash sinter using conventional flash methods, are the most stable materials when processed by the NSFSPS method. The TCR that decreases the heat flowing into the lateral punch/die interface is the main factor explaining the high-temperature concentration inside the NSFSPS

setup's central column independently of the sample material nature. The heat generated by the central column is contained in the sample, which helps reducing the temperature gradients within the sample. The higher the TCR is, the more homogeneous are the sample temperatures and the more homogeneous are the respective microstructures. The thermal confinement and the short sintering time are favorable conditions to ensure the microstructure homogeneity observed experimentally. The thermal confinement results also from the lateral graphite foil heating. For ceramics samples, a significant amount of the electric current is constrained in the sample/die graphite foil. Under these conditions, the lateral graphite foil can be compared to a susceptor that heats the sample from the edge and considerably stabilizes the sample temperature homogeneity. The forced thermal runaway generates heating rates of 1700 K min^{-1} for nickel and 4300 K min^{-1} for alumina. For zirconia, the transition regime occurs at a sample temperature of 1250 °C, where the heating rate passes from 3400 K min^{-1} to 12000 K min^{-1}. This transition is a result of an intrinsic thermal runaway that is added to the imposed electric current amplification. The differences between NSFSPS and traditional flash sintering should be mentioned. During NSFSPS, the applied pressure accelerates and stabilizes the overall sintering process. A die is used for a better control of the final sample shape of the sample. The NSFSPS method allows extending flash sintering to nearly all materials, controlling sample shape by an added graphite die, and an energy efficient mass production of small and intermediate size objects.

One of the key problems in the processing of ceramics is the requirement of high temperatures needed for sintering and densification. High-temperature sintering equipment is costly, while the processing requires inputs of large amounts of energy. The main advantage of flash sintering is a dramatic reduction of the processing time and temperature, as was illustrated by many examples. Flash sintering has been proven successful for densification of $K_{0.5}Na_{0.5}NbO_3$, a promising lead-free ferroelectric material [43]. A flash sintering process 30 s long at 990 °C was shown to produce a material with a high relative density (94%). In order to achieve the same relative density by conventional sintering, the process should be carried out at 1100 °C for 2 h. Flash sintering at a low furnace temperature of less than 100 °C was reported for $La_{0.6}Sr_{0.4}Co_{0.2}Fe_{0.8}O_3$ under electric fields of 7.5–12.5 $V \cdot cm^{-1}$ [47] – an extraordinary effect caused by a high electrical conductivity of the material.

Materials that have been processed by flash sintering in different laboratories have been classified by Yu et al. [1] using the conductivity mode – ionic conductors, metallic-like conductors, semiconductors, and insulators. Yu et al. [1] see the reason for a limited number of studies of the properties of flash-sintered materials in the small size of the samples dictated by the requirements of the method (application of field and placing samples into a furnace). At the same time, the potential of flash sintering has been proven for different structural and functional materials: lightweight ceramics, materials for solid-state electrochemical devices, ferroelectric materials, and dielectrics, as reviewed by Yu et al. [1]. Recent studies have shown that thermoelectric materials can also be produced by flash sintering: Du et al. [42] found that by switching from conventional SPS in a die to flash SPS without a die, it is possible to produce magnesium silicide stannide materials with altered electrical

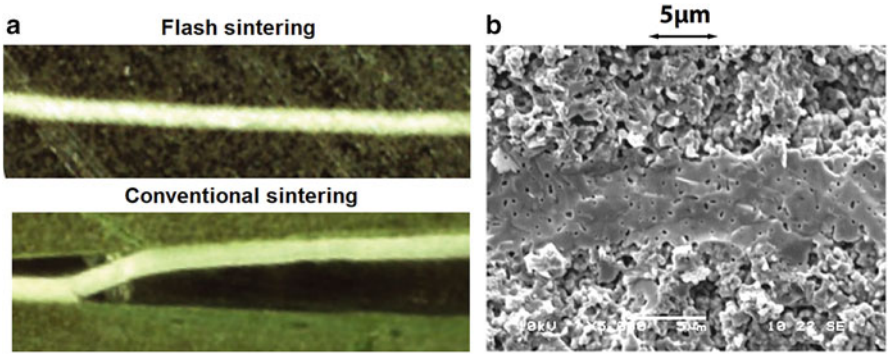

Fig. 5.36 Multilayers NiO–ZrO_2/cubic ZrO_2 sintered by flash and conventional sintering, the bright band in the middle is the electrolyte layer (**a**), the structures of the anode and electrolyte layers sintered and joined by flash sintering (**b**). (Reprinted from Francis et al. [48], Copyright (2013) with permission of John Wiley & Sons)

and thermal conductivities due to local melting-induced phase and structural changes.

Layered structures composed of an anode material (NiO-zirconia) and cubic zirconia electrolyte – structures for solid oxide fuel cell applications – were successfully flash sintered at 915 °C and 150 $V \cdot cm^{-1}$ using as assembly, in which the anode and the electrolyte layers were connected electrically in parallel [48]. The key problem in manufacturing of oxide fuel cells is sintering of the ceramic anode, electrolyte, and cathode layers, as sintering of one layer constrains sintering of the other. Co-sintered layers usually suffer from delamination and defects due to different sintering rates of the layers. In Ref. [48], the flash sintering temperature of the multilayer structure was lower than the temperature at which the anode material sinters when processed separately (1005 °C). The electrolyte as a separate layer sinters at 750 °C. The electrolyte had a high relative density and showed only closed pores, while the anode layer was porous, which is required for solid oxide fuel cells. The flash-sintered multilayers were free from defects and did not show delamination, unlike conventionally sintered multilayers (Fig. 5.36). The experimental results suggested that the behavior of the multilayers during flash sintering was a result of the interaction between the layers, and it was not possible to predict the flash sintering outcome by simply considering the behavior of the individual layers. As flash sintering helped alleviate the problems associated with constrained sintering, it was concluded to be a promising method for fabricating layered structures, such as those required for manufacturing of solid oxide fuel cells.

Studies focusing on comparison of the properties of materials of the same composition produced by sintering in different modes are valuable from the fundamental and practical viewpoints, as they shed light on the mechanisms a certain property is achieved under varied sintering conditions and allow formulating recommendations on the choice of the sintering modes for the material fabrication. Jesus et al. [49] reported the dependences of the grain size and the dielectric constant

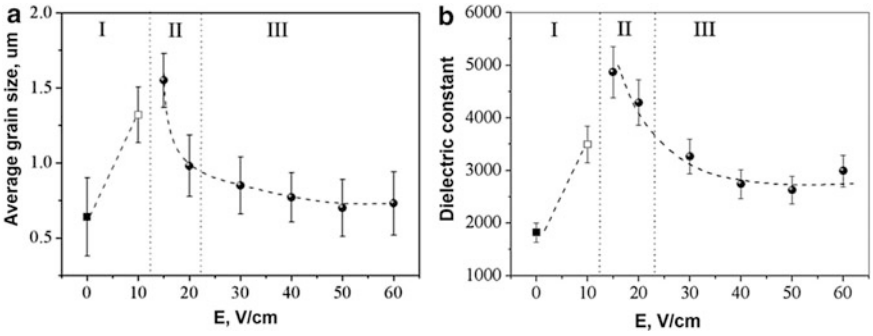

Fig. 5.37 Grain size (**a**) and dielectric constant measured at room temperature at 1 MHz (**b**) of $CaCu_3Ti_4O_{12}$ sintered using different field strength, which determined the sintering mode: conventional-like (region I), field-assisted (region II), flash-dominated (region III). (Reprinted from Jesus et al. [49], Copyright (2016) with permission from Elsevier)

of the sintered $CaCu_3Ti_4O_{12}$ on the field strength, which determined the sintering mode: conventional-like (region I), field-assisted (region II), flash-dominated (region III), as is shown in Fig. 5.37. The specimens were cold-pressed to a density of 55%, suspended on platinum wires, which served as field and current carrying electrodes, and placed into a furnace. The grain size correlated with the dielectric constant showing that under the selected measurement conditions, the dielectric constant of the sintered materials is modulated by the grain-boundary response.

An interesting result of flash sintering was reported in Ref. [50] for the phase transformation in the 3 mol.%Y_2O_3-ZrO_2 system. The powder heat treated at 600 °C contained monoclinic zirconia; conventional sintering at 1100 °C for 1 h led to a partial phase transformation into the tetragonal phase (Fig. 5.38a–b), which showed that prolonged annealing is needed to achieve the formation of a single-phase product from the 3 mol.%Y_2O_3-ZrO_2 mixture. Unlike conventional sintering, flash sintering was very efficient in transforming the mixture into single-phase tetragonal zirconia (Fig. 5.38c–d). However, the effect of electric field during flash sintering on the phase transformation rate remains unclear. Both the bulk and intrinsic grain-boundary conductivity increased with increasing holding time during flash sintering. The estimated grain-boundary thickness δ_{gb} and intrinsic (specific) conductivity σ_{gb}^{sp} of the grain boundary ($\sigma_{gb} = \frac{D_g}{\delta_{gb}}\sigma_{gb}^{sp}$, where D_g is the grain size) are shown in Fig. 5.39. Based on these results, it was concluded that flash sintering created oxygen vacancies in both grains and grain boundaries that accumulated during the holding time.

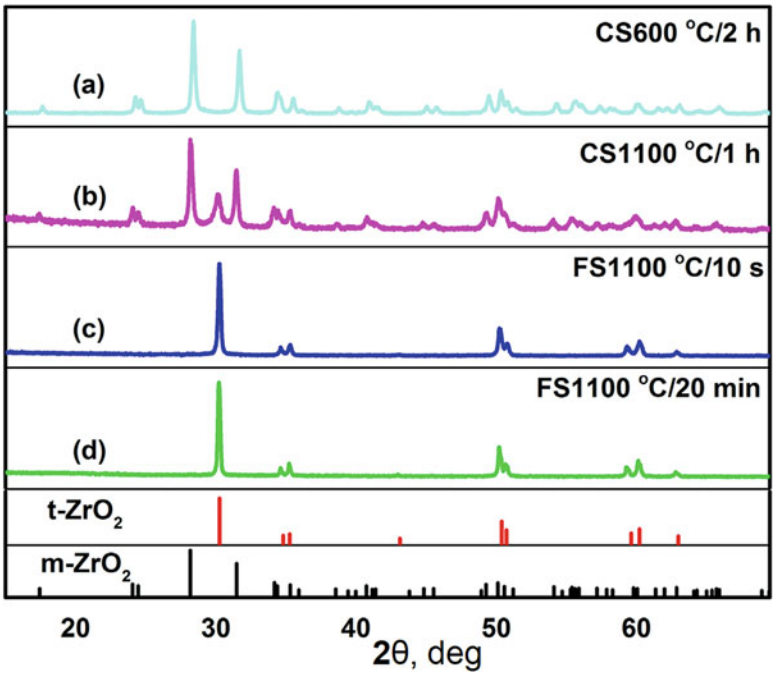

Fig. 5.38 XRD patterns of the 3 mol.%Y_2O_3-ZrO_2 powder heat treated at 600 °C for 2 h (**a**), compact pre-sintered at 1100 °C for 1 h (**b**) and compacts flash sintered at 1100 °C with holding times of 10 s (**c**) and 20 min (**d**). (Reprinted from Liu et al. [50], Copyright (2016) with permission of Elsevier)

5.4 Summary

Flash sintering is a fascinating physical phenomenon, which also offers significant energy saving and shortening of processing times. "Traditional" flash sintering occurs when an electrical potential is applied to a pre-compacted specimen heated in a furnace. The characteristic field strength and power dissipation values in flash sintering are 100–100 $V \cdot cm^{-1}$ and 10–1000 $W \cdot cm^{-3}$, respectively. "Traditional" flash sintering is accompanied by a sudden increase in the conductivity of the sintered material, while the temperature instability plays a crucial role in the development of flash sintering. Flash sintering can be initiated by arc plasma and microwave radiation. It is now recognized that all types of materials can be flash sintered regardless of their electrical conductivity evolution with temperature if thermal runaway is forced in the sample through tailoring the electric current pattern.

Although possibilities of fast densification of pre-consolidated compacts via flash sintering have been reported for a wide range of materials, structural analyses of the densified materials have been followed by the detailed property testing only in a limited number of studies. The question of specific properties of materials whose

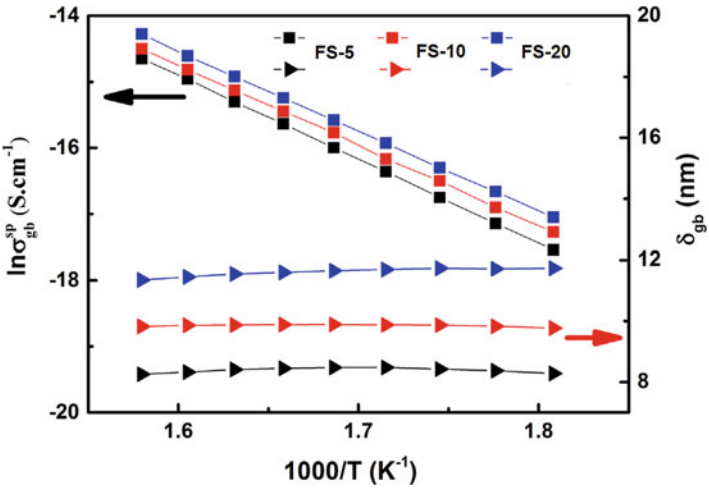

Fig. 5.39 Estimated grain-boundary thickness and intrinsic conductivity of the grain boundary as a function of temperature for flash-sintered 3 mol.%Y_2O_3-ZrO_2 (FS-5, holding time 5 min; FS-10, holding time 10 min; FS-20, holding time 20 min). (Reprinted from Liu et al. [50], Copyright (2016) with permission of Elsevier)

grain boundaries experienced melting as a result of flash sintering is extremely important from the fundamental point of view of the field-induced materials transformations and from a technological perspective of producing materials with advanced properties by energy- and time-saving routes. Until now, most of the flash sintering studies focused on the single-phase materials. At the same time, the role of additives in the processes has been demonstrated, and the behavior of layered structure under flash sintering has been shown to be better compared with conventional sintering in terms of the absence of delamination. For the future research, multiphase materials present interesting and challenging objects to apply the flash sintering approach to, as the phases will most probably differ in electrical conductivity and the character of its evolution with temperature.

By and large, flash sintering emerges as a remarkable way to consolidate powder materials within extremely short periods of time. While the overall process duration may vary due to the presence of the heating and cooling parts of the sintering cycle, the actual time of densification in many cases is less than several seconds. The ability to subject materials to flash sintering has already been demonstrated for a broad variety of materials and for various field-assisted sintering techniques, including the most traditional free pressureless version of flash sintering assisted by an applied DC voltage, flash spark plasma sintering, and flash microwave sintering. While most of flash sintering experiments have been conducted for ceramic materials, it was shown that metals can be flash sintered too, when the "flash" is triggered initially by a ceramic tooling.

From the fundamental research perspective, the underlying physical mechanisms of flash sintering are currently actively debated. While the most active discussion is

related to the acceptance or rejection of the thermal runaway phenomena during flash sintering, less attention is paid to the nature of ultra-rapid densification itself. Indeed, it is still not clear, whether the achievement of very high temperature can explain almost instantaneous densification of many material systems.

From the applied research perspective, the main issues are the stability of flash sintering and the related questions of its scalability. Thus, flash sintering is one of the brightest examples of the importance of *the control of non-equilibrium*, which is a major issue for most field-assisted sintering techniques.

References

1. Yu M, Grasso S, Mckinnon R, Saunders T, Reece MJ (2017) Review of flash sintering: materials, mechanisms and modeling. Adv Appl Ceram 116:24–60
2. Cologna M, Rashkova B, Raj R (2010) Flash sintering of nanograin zirconia in < 5 s at 850 degrees C. J Am Ceram Soc 93:3556–3559
3. Francis JSC, Cologna M, Raj R (2012) Particle size effects in flash sintering. J Eur Ceram Soc 32:3129–3136
4. Raj R (2012) Joule heating during flash-sintering. J Eur Ceram Soc 32:2293–2301
5. Saini KK, Sharma CP, Chanderkant SDK, Ravat KB, Chandra S, Tewari SP (1993) Effect of thallium concentration on Tl-2201 superconducting phase by flash sintering process. Physica C 216:59–65
6. Muccillo R, Muccillo ENS (2013) An experimental setup for shrinkage evaluation during electric field-assisted flash sintering: application to yttria-stabilized zirconia. J Eur Ceram Soc 33:515–520
7. Hao X, Liu Y, Wang Z, Qiao J, Sun K (2012) A novel sintering method to obtain fully dense gadolinia doped ceria by applying a direct current. J Power Sources 210:86–91
8. Muccillo R, Kleitz M, Muccillo ENS (2012) Flash grain welding in yttria stabilized zirconia. J Eur Ceram Soc 31:1517–1521
9. Cologna M, Prette ALG, Raj R (2011) Flash-sintering of cubic yttria-stabilized zirconia at 750 degrees C for possible use in SOFC manufacturing. J Am Ceram Soc 94:316–319
10. Prette ALG, Cologna M, Sglavo V, Raj R (2011) Flash-sintering of Co_2MnO_4 spinel for solid oxide fuel cell applications. J Power Sources 196:2061–2065
11. Cologna M, Francis JSC, Raj R (2011) Field assisted and flash sintering of alumina and its relationship to conductivity and MgO-doping. J Eur Ceram Soc 31:2827–2837
12. Zapata-Solvas E, Bonilla S, Wilshaw PR, Todd RI (2013) Preliminary investigation of flash sintering of SiC. J Eur Ceram Soc 33:2811–2816
13. Saunders T, Grasso S, Reece MJ (2016) Ultrafast-contactless flash sintering using plasma electrodes. Sci Rep 6:27222
14. Grasso S, Saunders T, Porwal H, Cedillos-Barraza O, Jayaseelan DD, Lee WE, Reece MJ (2014) Flash spark plasma sintering (FSPS) of pure ZrB_2. J Am Ceram Soc 97(8):2405–2408
15. Olevsky EA, Rolfing SM, Maximenko AL (2016) Flash (ultra-rapid) spark-plasma sintering of silicon carbide. Sci Rep 6:33408
16. Grasso S, Saunders T, Porwal H, Milsom B, Tudball A, Reece M (2016) Flash spark plasma sintering (FSPS) of α and β SiC. J Am Ceram Soc 99(5):1534–1543
17. Grasso S, Kim EY, Saunders T, Yu M, Tudball A, Choi SH, Reece M (2016) Ultra-rapid crystal growth of textured SiC using flash spark plasma sintering route. Cryst Growth Des 16:2317–2321
18. McWilliams B, Yu J, Kellogg F, Kilczewski S (2017) Enhanced sintering kinetics in aluminum alloy powder consolidated using DC electric fields. Metall Mater Trans A 48:919–929

19. Zhang Y, Luo J (2015) Promoting the flash sintering of ZnO in reduced atmospheres to achieve nearly full densities at furnace temperatures of <120 deg C. Scr Mater 106:26–29
20. Hewitt IJ, Lacey AA, Todd RI (2015) A mathematical model for flash sintering. Math Model Nat Phenom 10(6):77–89
21. Dong Y, Chen IW (2016) Thermal runaway in mold-assisted flash sintering. J Am Ceram Soc 99(9):2889–2894
22. Dong Y, Chen IW (2015) Predicting the onset of flash sintering. J Am Ceram Soc 98 (8):2333–2335
23. Dong Y, Chen IW (2015) Onset criterion for flash sintering. J Am Ceram Soc 98 (12):3624–3627
24. Downs JA, Sglavo VM (2013) Electric field assisted sintering of cubic zirconia at 390°C. J Am Ceram Soc 96(5):1342–1344
25. Francis JSC, Raj R (2012) Flash-sinterforging of nanograin zirconia: field assisted sintering and superplasticity. J Am Ceram Soc 95:138–146
26. Raj R, Cologna M, Francis JSC (2011) Influence of externally imposed and internally generated electrical fields on grain growth, diffusional creep, sintering and related phenomena in ceramics. J Am Ceram Soc 94:1941–1965
27. Karakuscu A, Cologna M, Yarotski D, Won J, Francis JSC, Raj R, Uberuaga BP (2012) Defect structure of flash-sintered strontium titanate. J Am Ceram Soc 95:2531–2536
28. Grasso S, Sakka Y, Rendtorff N, Hu CF, Maizza G, Borodianska H, Vasylkiv O (2011) Modeling of the temperature distribution of flash sintered zirconia. J Ceram Soc Jap 119:144–146
29. Park J, Chen IW (2013) In situ thermometry measuring temperature flashes exceeding 1,700°C in 8 Mol% Y_2O_3-stablized zirconia under constant-voltage heating. J Am Ceram Soc 96:697–700
30. Todd RI, Zapata-Solvas E, Bonilla RS, Sneddon T, Wilshaw PR (2015) Electrical characteristics of flash sintering: thermal runaway of joule heating. J Eur Ceram Soc 35:1865–1877
31. Narayan J (2013) A new mechanism for field-assisted processing and flash sintering of materials. Scr Mater 69:107–111
32. Bykov YV, Egorov SV, Eremeev AG, Kholoptsev VV, Plotnikov IV, Rybakov KI, Sorokin AA (2016) On the mechanism of microwave flash sintering of ceramics. Materials 9:684
33. Bykov YV, Egorov SV, Eremeev AG, Kholoptsev VV, Rybakov KI, Sorokin AA (2015) Flash microwave sintering of transparent Yb:$(LaY)_2O_3$ ceramics. J Am Ceram Soc 98(11):3518–3524
34. Chaim R (2016) Liquid film capillary mechanism for densification of ceramic powders during flash sintering. Materials 9:280
35. Chaim R (2017) Particle surface softening as universal behavior during flash sintering of oxide nano-powders. Materials 10:179
36. Candelario VM, Moreno R, Todd RI, Ortiz AL (2017) Liquid-phase assisted flash sintering of SiC from powder mixtures prepared by aqueous colloidal processing. J Eur Ceram Soc 37:485–498
37. Lebrun JM, Morrissey TG, Francis JSC, Seymour KC, Kriven WM, Raj R (2015) Emergence and extinction of a new phase during on–off experiments related to flash sintering of 3YSZ. J Am Ceram Soc 98:1493–1497
38. Jha SK, Lebrun JM, Seymour KC, Kriven WM, Raj R (2016) Electric field induced texture in titania during experiments related to flash sintering. J Eur Ceram Soc 36(1):257–261
39. Perelaer J, Klokkenburg M, Hendriks CE, Schubert US (2009) Microwave flash sintering of inkjet-printed silver tracks on polymer substrates. Adv Mater 21:4830–4834
40. Perelaer J, Jani R, Grouchko M, Kamyshny A, Magdassi S, Schubert US (2012) Plasma and microwave flash sintering of a tailored silver nanoparticle ink, yielding 60% bulk conductivity on cost-effective polymer foils. Adv Mater 24:3993–3998
41. Manière C, Lee G, Zahrah T, Olevsky EA (2018) Microwave flash sintering of metal powders: from experimental evidence to multiphysics simulation. Acta Mater 147:24–34

42. Du B, Gucci F, Porwal H, Grasso S, Mahajan A, Reece MJ (2017) Flash spark plasma sintering of magnesium silicide stannide with improved thermoelectric properties. J Mater Chem C 5:1514–1521
43. Corapcioglu G, Ali Gulgun M, Kisslinger K, Sturm S, Jha SK, Raj R (2016) Microstructure and microchemistry of flash sintered $K_{0.5}Na_{0.5}NbO_3$. J Ceram Soc Japan 124(4):321–328
44. Biesuz M, Luchi P, Quaranta A, Sglavo VM (2016) Theoretical and phenomenological analogies between flash sintering and dielectric breakdown in a-alumina. J Appl Phys 120:145107
45. Manière C, Lee G, Olevsky EA (2017) All-materials-inclusive flash spark plasma sintering. Sci Rep 7:15071
46. Zapata-Solvas E, Gómez-García D, Domínguez-Rodríguez A, Todd RI (2015) Ultra-fast and energy-efficient sintering of ceramics by electric current concentration. Sci Rep 5:8513
47. Gaur A, Sglavo VM (2014) Densification of $La_{0.6}Sr_{0.4}Co_{0.2}Fe_{0.8}O_3$ ceramic by flash sintering at temperature less than 100 °C. J Mater Sci 49:6321–6332
48. Francis JSC, Cologna M, Montinaro D, Raj R (2013) Flash sintering of anode–electrolyte multilayers for SOFC applications. J Am Ceram Soc 96(5):1352–1354
49. Jesus LM, Santos Silva R, Raj R, M'Peko JC (2016) Electric field-assisted flash sintering of $CaCu_3Ti_4O_{12}$: microstructure characteristics and dielectric properties. J Alloys Comp 682:753–758
50. Liu D, Gao Y, Liu J, Wang Y, An L (2016) Effect of holding time on the microstructure and properties of flash sintered Y_2O_3-doped ZrO_2. Ceram Int 42:17442–17446